Chemosphere 297 (2022) 134166

Contents lists available at ScienceDirect

Chemosphere

journal homepage: www.elsevier.com/locate/chemosphere

Impact on air quality of carbon and sulfur volatile compounds emitted from hydrothermal discharges: The case study of Pisciarelli (Campi Flegrei, South Italy)

R. Biagi [a,*], F. Tassi [a,b], S. Caliro [c], F. Capecchiacci [a,c], S. Venturi [a,b]

[a] Department of Earth Sciences, University of Florence, Via G. La Pira 4, 50121, Firenze, Italy
[b] Institute of Geosciences and Earth Resources (IGG), National Research Council of Italy (CNR), Via G. La Pira 4, 50121, Firenze, Italy
[c] Istituto Nazionale di Geofisica e Vulcanologia (INGV), Sezione di Napoli, Osservatorio Vesuviano, Via Diocleziano 328, 80124, Napoli, Italy

HIGHLIGHTS

- CO_2, CH_4, H_2S, SO_2 mole fractions in air, and $\delta^{13}C$ isotopes, were measured in Pisciarelli.
- CO_2 and H_2S concentrations in air were mainly related to the hydrothermal system emissions.
- CO_2 mixed with both the local background and anthropogenic sources.
- CH_4 emissions were likely governed by anthropogenic sources from the city.
- SO_2 concentrations were governed both from consumption of H_2S and anthropogenic sources.

GRAPHICAL ABSTRACT

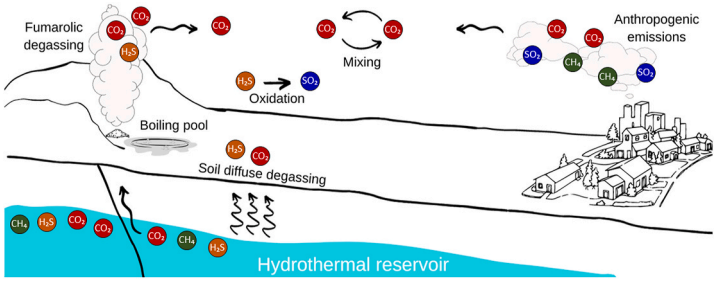

ARTICLE INFO

Handling Editor: Volker Matthias

Keywords:
Hydrothermal systems
Air quality
Carbon and sulfur volatile compounds
Carbon isotopes
Natural sources of pollutants.

ABSTRACT

Volcanoes are currently to be regarded as natural sources of air pollutants. Climatic and environmental forcing of large volcanic eruptions are well known, although gases emitted through passive degassing during periods of quiescence or hydrothermal activity can also be highly dangerous for the environment and public health. Based on compositional and isotopic data, a survey on the spatial distribution in air of the main volatile compounds of carbon (CO_2 and CH_4) and sulfur (H_2S and SO_2) emitted from the fumarolic field of Pisciarelli (Campi Flegrei, Pozzuoli, Naples), a hydrothermal area where degassing activity has visibly increased since 2009, was carried out. The main goals of this study were (i) to evaluate the impact on air quality of these natural manifestations and (ii) inquire into the behavior of the selected chemical species once released in air, and their possible use as tracers to distinguish natural and anthropogenic sources. Keeling plot analysis of CO_2 and CH_4 isotopes revealed that the hydrothermal area acts as a net source of CO_2 in air, whilst CH_4 originated mainly from anthropogenic sources. Approaching the urban area, anthropogenic sources of CO_2 increased and, at distances greater than 800 m from the Pisciarelli field, they prevailed over the hydrothermal signal. While hydrothermal CO_2 simply mixed with that in the atmospheric background, H_2S was possibly affected by oxidation processes. Therefore, SO_2 measured in the air near the hydrothermal emissions had a secondary origin, i.e. generated by oxidation of hydrothermal H_2S. Anthropogenic SO_2 was recognized only in the furthest measurement site from Pisciarelli. Finally, in the proximity of a geothermal well, whose drilling was in progress during our field campaign, the H_2S concentrations

* Corresponding author.
E-mail address: rebecca.biagi@unifi.it (R. Biagi).

https://doi.org/10.1016/j.chemosphere.2022.134166
Received 30 November 2021; Received in revised form 21 February 2022; Accepted 26 February 2022
Available online 1 March 2022

have reached values up to 3 orders of magnitude higher than the urban background, claiming the attention of the local authorities.

1. Introduction

Air pollution poses a serious hazard to public health and environment. According to the World Health Organization (WHO), deaths caused by exposure to polluted air were around 4.2 million worldwide in 2016, while 90% of people live in places where concentrations of pollutants in the air exceed the recommended threshold values (WHO, 2018). Air pollutants from anthropogenic activity are regarded as the main causes of global scale phenomena having a dramatic impact on ecosystems and human health, such as greenhouse effect, the ozone hole, and acid rain, (McCormick et al., 1995; Robock, 2000; Monks et al., 2009; Burton et al., 2013).

Volcanoes are significant sources of air pollutants, such as trace elements (Calabrese et al., 2016, and references therein) and acid gases (Reikard, 2019, and references therein). Magmas contain dissolved volatiles (mostly consisting of water vapor, CO_2 and SO_2) that are released in large quantities during (i) volcanic eruptions (e.g., Robock, 2004; Self, 2005) and (ii) long periods of quiescence through a persistent diffuse degassing or fumarolic vents (e.g., Mörner and Etiope, 2002; Aiuppa, 2015; Cardellini et al., 2017). Water vapor and CO_2 are regarded as two of the main greenhouse gases, whereas SO_2 and H_2S, the latter being mainly produced by SO_2 reduction in a hydrothermal environment, react in air with hydroxyl radicals (OH) and water vapor producing H_2SO_4 that forms aerosol that reflects solar radiation, causing a generalized cooling of the troposphere and the warming of the stratosphere (Rampino and Self, 1982; Self et al., 1993; McCormick et al., 1995). Sulfur-bearing volatiles also contribute to (i) the degradation of the ozone layer, (ii) production of acid rain, and (iii) air pollution known as "volcanic smog" or "vog" (McGee et al., 1997; Andres and Kasgnoc, 1998; Robock, 2000; Textor et al., 2003; von Glasow et al., 2009).

Most studies focused on the environmental and climatic impacts and the associated risks of large eruptions (e.g. Robock, 1981; Kelly and Sear, 1984; Allard et al., 1991; Hansen et al., 1992; Self et al., 1993; McCormick et al., 1995; Robock, 2000; Oppenheimer, 2003; Textor et al., 2003; Robock, 2004; Self et al., 2004; Self, 2005; Horwell and Baxter, 2006; Self, 2006; von Glasow et al., 2009; Gerlach, 2011; Raible et al., 2016), whereas little is known about the fate of gases emitted during the long-lasting non-eruptive periods and hydrothermal activity. Recent studies have shown that volcanoes emit to the atmosphere a huge amount of volatiles even during quiescent periods (Baubron et al., 1990; Allard et al., 1991; Delmelle et al., 2002; Mörner and Etiope, 2002). For instance, Mount Etna (Sicily, South Italy) emits about 21×10^9 g day^{-1} of TV (Total Volatile) (Aiuppa et al., 2008); Stromboli Island (Aeolian Islands, South Italy) $6–12 \times 10^9$ g day^{-1} (Allard et al., 1994) and the volcano Masaya (Nicaragua) $14–16 \times 10^9$ g day^{-1} (Burton et al., 2000; Martin et al., 2010; Girona et al., 2014).

Campi Flegrei caldera (CFc) in southern Italy, one of the most active volcanic complexes of the Mediterranean area, hosts the densely populated Pozzuoli town (1,844 inhabitants per square kilometer in 2019; AdminStat, 2020), thus representing one of the most prominent examples of coexistence of human settlements with active volcanic systems. CFc is currently showing an intense hydrothermal activity, mostly occurring (i) at the Solfatara Crater and (ii) in an area approximately 400 m eastward from Solfatara namely Pisciarelli, where the hydrothermal discharge rate has strongly increased in the last decade (Chiodini et al., 2015, 2017; Tamburello et al., 2019).

In this study, we present the results of a geochemical survey carried out at five sites near the Pisciarelli hydrothermal field, where high-frequency measurements in air of CO_2, CH_4, SO_2 and H_2S concentrations, and $\delta^{13}C–CO_2$ and $\delta^{13}C–CH_4$ values were performed. The main aim was to investigate the spatial distribution of the gases emitted in air from the Pisciarelli hydrothermal discharges in order to (i) evaluate their impact on air quality and (ii) enquire into the behavior of the selected chemical species once released in air, and their possible use as tracers to distinguish natural (hydrothermal) and anthropogenic sources.

2. Study area

The Phlegrean Volcanic District is a volcanic complex of alkali-potassic affinity (Florio et al., 1999) located along the Tyrrhenian margin, NW of Naples (Italy). It consists of a series of monogenic volcanic edifices, including the islands of Procida and Ischia, and submarine vents in the northwestern Gulf of Naples (Orsi et al., 1996). The morpho-structural setting is dominated by collapsed structures produced during two main eruptive events: (i) the Campanian Ignimbrite eruption (39 ka; De Vivo et al., 2001), which formed a first caldera, and (ii) the Neapolitan Yellow Tuff eruption, which caused a further collapse about 14.9 ka (Orsi et al., 1996, 2004; Deino et al., 2004). The last eruptive activity occurred in 1538 A.D. (Monte Nuovo eruption; Di Vito et al., 1987; Orsi et al., 1996), whereas bradyseismic crises occurred in 1970–72 and 1982–84 (Barberi et al., 1984; Bonafede and Mazzanti, 1998), the latter causing ground uplifts up to 3.5 m, a situation that imposed the evacuation of more than 40,000 people in 1984 (Barberi et al., 1984; De Vivo et al., 2001). These slow vertical ground movements were accompanied by thousands of earthquakes with epicenters at the Solfatara Crater (Vilardo et al., 1991), a 1.4 km^2-wide tuff cone (Fig. 1a) produced about 4 ka from a low-magnitude eruption (Isaia et al., 2009).

Solfatara crater hosts the most prominent hydrothermal discharges in CFc (Chiodini et al., 2012; Cardellini et al., 2017), whose deep source (2,000–2,500 m depth) is a liquid-dominated aquifer at $\geq$ 360 °C and 200–250 bar, overlain by a vapor-dominated zone at 200–240 °C (Caliro et al., 2007, and references therein). Pisciarelli, located approximately 400 m eastward of the Solfatara Crater, is a 0.03 km^2 hydrothermal fault-related system (67 m a.s.l.) including several high-flow fumaroles and boiling pools (Fig. 1b). In this site, a significant increase of both shallow seismicity and hydrothermal activity has recently been observed, as testified by the opening of a new fumarolic vent in 2009 emitting a $H_2O–CO_2$ rich gas mixture, with minor H_2S, at temperatures up to 114 °C (Chiodini et al., 2015; Tamburello et al., 2019). Recent studies (Aiuppa et al., 2013; Queiβer et al., 2017; Tamburello et al., 2019) have shown that the fluid output from Pisciarelli in the last years accounts for several kilotons for day, with >29 MW of energy being released from only the 2009 fumarole.

Hydrothermal diffuse emissions and weak fumaroles occur along the Antiniana street, a densely urbanized sector of CFc located about 1 km south of Pisciarelli in the Agnano crater (Fig. 1b). In this area, two geothermal wells are also present (Fig. 1b), one abandoned and showing a low flow rate, the other, characterized by a strong flow rate, drilled in June 2020 (INGV-OV, 2020).

3. Materials and methods

3.1. Measurement strategy

Carbon- and sulfur-bearing pollutants in air were measured in January and June 2020. During the first campaign, the measurements were carried out at four sites, as follows: (i) FU ("Fumaroles"), (ii) AC ("Artificial Conduit"), (iii) HT ("Hotel Tennis"), and (iv) DS ("Distal Site") (Fig. 1b). During the second campaign, the measurements were (i)

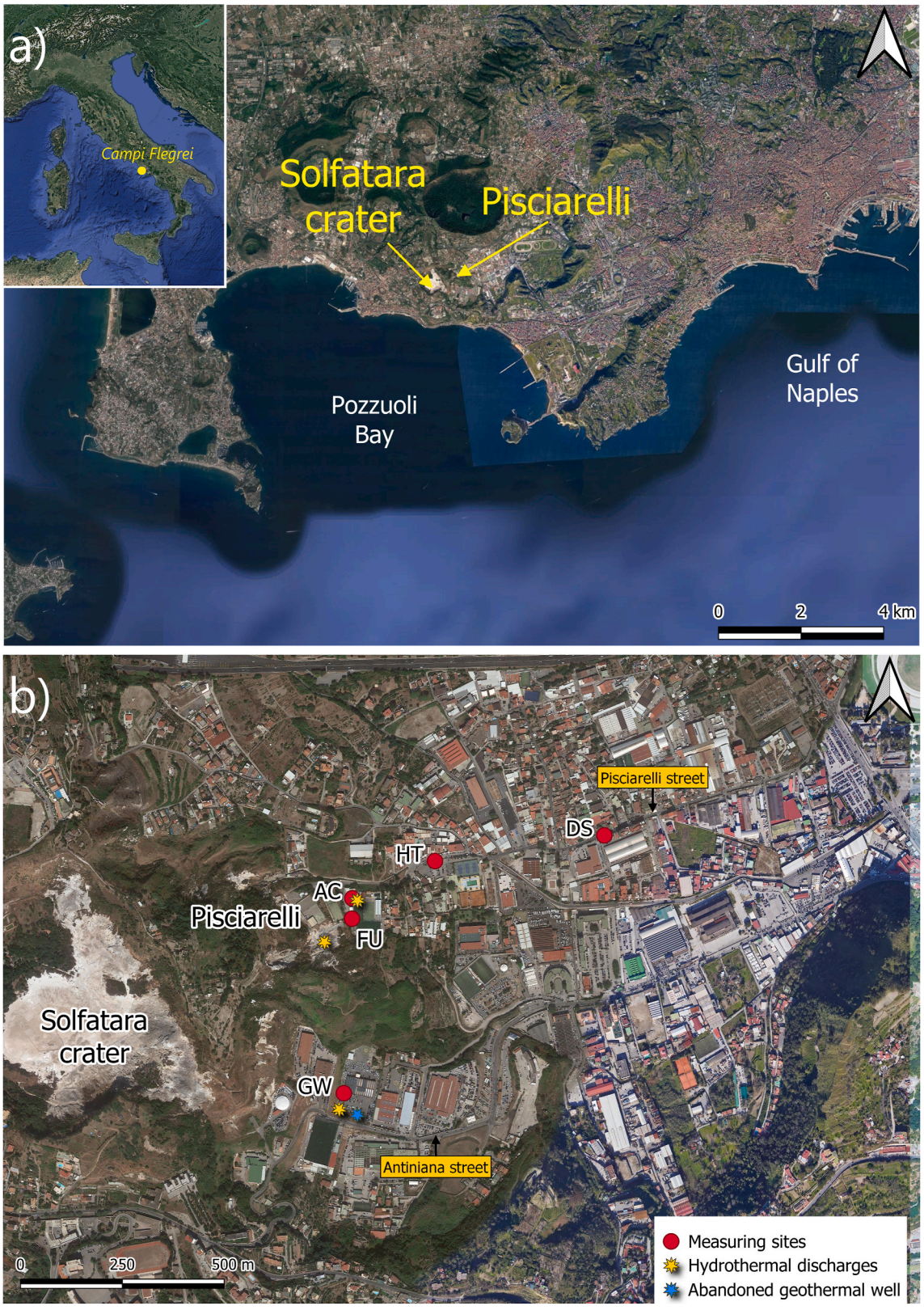

Fig. 1. (a) Satellite image of Campi Flegrei area, with location of Solfatara crater and Pisciarelli hydrothermal fields. (b) Location of measuring sites (red dots), hydrothermal discharges (orange stars) and the abandoned geothermal well along Antiniana street (light blue star). (For interpretation of the references to colour in this figure legend, the reader is referred to the Web version of this article).

performed at the GW ("Geothermal Well") site, and (ii) repeated at the AC site.

The FU site was the closest one (about 85 m; Fig. 1b) to the main hydrothermal discharges of Pisciarelli, whereas the AC site was at the entrance of a sport center (about 120 m from the Pisciarelli discharges; Fig. 1b) at few meters from a 2 m high cemented chimney that releases to the atmosphere hydrothermal fluids conveyed from the punctual and diffuse emissions buried under the concrete pavement and local infrastructures. The GW site was located within a car park along the Antiniana street, i.e. close (about 40 m) to the actively-drilled geothermal well (Fig. 1b). The HT site was situated inside the parking lot of a hotel, at about 325 m from the main Pisciarelli hydrothermal discharges (Fig. 1b). Noteworthily, the parking lot hosts a wastewater tank, discharging vapors at relatively high rate. The DS site was the farthest one (about 800 m) from the main Pisciarelli hydrothermal discharges (Fig. 1b). It was located along Pisciarelli street, a vehicular road connecting the homonymous locality (belonging to the Municipality of Pozzuoli) to Agnano (part of the 10th Municipality of Naples).

Timing and duration of the measurement sessions carried out at each site are reported in Table 1.

3.2. Instrumental equipment and data acquisition

CO_2 and CH_4 concentration (in mg/m^3) and the $\delta^{13}C$–CO_2 and $\delta^{13}C$–CH_4 values (in ‰ vs. V-PDB) were measured by WS-CRDS (Wavelength-Scanned Cavity Ring-Down Spectroscopy) using a Picarro

Table 1
Summary descriptive statistical parameters on the minute-averaged data measured at each site, and meteorological parameters (WD = wind direction, WS = wind speed).
Chemical compositions of CO_2 and CH_4 are in mg/m^3; chemical compositions of H_2S and SO_2 are in μg/m^3; $\delta^{13}C$–CO_2 and $\delta^{13}C$–CH_4 are in ‰ vs. V-PDB; WS (minimum-maximum) are in km/h.

Site	Distance	Date	Parameter	Start	Stop	Min	Max	Mean	SD	WD	WS
FU	85 m	January 22, 2020 (UTC+1)	CO_2	11:53	17:16	922	1,677	1,090	120	variable	3–8
			CH_4	11:53	17:16	1.41	1.46	1.43	0.009		
			$\delta^{13}C$–CO_2	11:53	17:16	−10.5	−5.9	−8.6	0.9		
			$\delta^{13}C$–CH_4	11:53	17:16	−49.8	−43.8	−45.9	0.88		
			SO_2	11:54	17:16	7.05	44	20	7.3		
			H_2S	11:54	17:16	94	1,333	362	184		
AC	120 m	January 21, 2020 (UTC+1)	CO_2	16:50	18:11	862	1,197	980	107	NE-NNE	13
			CH_4	16:50	18:11	1.39	1.40	1.40	0.003		
			$\delta^{13}C$–CO_2	16:50	18:11	−10.3	−7.3	−8.9	0.7		
			$\delta^{13}C$–CH_4	16:50	18:11	−49.3	−44.7	−47.0	0.75		
			SO_2	16:51	18:11	1.30	9.79	4.58	1.7		
			H_2S	16:51	18:11	0.78	82	10	12		
AC	120 m	June 09, 2020 (UTC+2)	CO_2	16:00	17:31	746	1,068	831	77	W	19–22
			CH_4	16:00	17:31	1.26	1.28	1.27	0.002		
			$\delta^{13}C$–CO_2	16:00	17:31	−9.5	−6.8	−8.4	0.6		
			$\delta^{13}C$–CH_4	16:00	17:31	−52.8	−48.5	−50.8	0.88		
			SO_2	15:12	17:48	3.26	29	10	5.4		
			H_2S	15:12	17:48	1.40	396	45	68		
GW	40 m	June 10, 2020 (UTC+2)	CO_2	10:30	12:47	792	1,061	884	53	W	11–24
			CH_4	10:30	12:47	1.29	1.31	1.30	0.003		
			$\delta^{13}C$–CO_2	10:30	12:47	−7.8	−6.2	−7.0	0.4		
			$\delta^{13}C$–CH_4	10:30	12:47	−51.2	−45.0	−48.6	1.17		
			SO_2	10:08	12:41	26	87	42	10.6		
			H_2S	10:08	12:41	250	1,570	497	188		
GW	40 m	June 10, 2020 (UTC+2)	CO_2	15:04	16:49	774	1,029	871	66	W	11–24
			CH_4	15:04	16:49	1.29	1.33	1.30	0.005		
			$\delta^{13}C$–CO_2	15:04	16:49	−7.9	−5.7	−6.9	0.5		
			$\delta^{13}C$–CH_4	15:04	16:49	−48.7	−44.1	−46.6	0.94		
			SO_2	15:04	16:42	13	84	37	15.5		
			H_2S	15:04	16:42	25	1,101	375	254		
GW	40 m	June 11, 2020 (UTC+2)	CO_2	9:40	10:49	777	1,052	864	55	SSW-SW	11–19
			CH_4	9:40	10:49	1.29	1.31	1.30	0.004		
			$\delta^{13}C$–CO_2	9:40	10:49	−8.0	−6.4	−7.2	0.4		
			$\delta^{13}C$–CH_4	9:40	10:49	−48.8	−45.4	−47.0	0.84		
			SO_2	9:19	10:42	9.10	42	20	8.6		
			H_2S	9:19	10:42	2.28	813	233	198		
HT	325 m	January 21-22, 2020 (UTC+1)	CO_2	23:20	10:25	1,087	2,109	1,567	230	N-NNE	5–11
			CH_4	23:20	10:25	1.41	1.63	1.45	0.05		
			$\delta^{13}C$–CO_2	23:20	10:25	−12.4	−5.8	−7.6	1.5		
			$\delta^{13}C$–CH_4	23:20	10:25	−50.4	−44.2	−46.3	0.85		
			SO_2	23:20	10:25	0.54	21	9.15	4.2		
			H_2S	23:20	10:25	10	618	192	126		
HT	325 m	January 22-23, 2020 (UTC+1)	CO_2	23:28	9:27	1,170	2,193	1,591	154	variable	<8
			CH_4	23:28	9:27	1.37	1.72	1.42	0.05		
			$\delta^{13}C$–CO_2	23:28	9:27	−11.4	−5.7	−7.3	1.0		
			$\delta^{13}C$–CH_4	23:28	9:27	−50.0	−45.2	−47.1	0.78		
			SO_2	23:28	9:29	u.d.l.	11	4.50	1.9		
			H_2S	23:28	9:29	5.83	126	44	29		
DS	800 m	January 23, 2020 (UTC+1)	CO_2	10:01	11:27	998	1,374	1,176	110	N-NE	3–5
			CH_4	10:01	11:27	1.54	2.23	1.69	0.14		
			$\delta^{13}C$–CO_2	10:01	11:27	−14.3	−12.5	−13.6	0.4		
			$\delta^{13}C$–CH_4	10:01	11:27	−49.9	−44.8	−47.8	1.10		
			SO_2	10:01	10:52	11	92	23	15		
			H_2S	10:01	10:52	27	91	52	16		

G2201-*i* analyzer, which reports 1 measure per second. Calibration was performed at the beginning of the two measuring periods using the following standards (Air Liquide): (i) 695, 915 and 1830 mg/m^3 CO_2, (ii) 1.2, 3.3 and 6.7 mg/m^3 CH_4, (iii) −44, −5 and +2‰ $\delta^{13}C$–CO_2, and (iv) −60 and −25‰ $\delta^{13}C$–CH_4 (Air Liquide). The precision was within 0.4 mg/m^3 (CO_2), 0.03 mg/m^3 (CH_4), 0.16‰ ($\delta^{13}C$–CO_2) and 1.15‰ ($\delta^{13}C$–CH_4). As suggested by Malowany et al. (2015), a copper-shavings trap was installed at the analyzer inlet port to minimize spectral interferences caused by high concentrations of H_2S, which could result in significant depletion in ^{13}C. H_2S and SO_2 concentrations (in μg/m^3) were measured by PF (Pulsed Fluorescence) using a Thermo® 450*i* analyzer (Thermo Fisher Scientific, 2012). The instrument, providing 1 measurement per min, has detection limits of 5.2 and 2.8 μg/m^3 for SO_2 and H_2S, respectively, and precision of ±1% (Venturi et al., 2016, 2019). Air samples were drawn through Teflon tubing using vacuum pumps with sampling rate of 25 mL min^{-1} and 70 mL min^{-1} for the Picarro and the Thermo, respectively. Minute-averages were obtained from the dataset acquired from each instrument and used for further data processing.

Meteorological parameters (wind speed, wind direction, humidity, and temperature) were also measured using a portable Kestrel® 4500 meteorological station (Kestrel®, 2020) which were integrated with those available online at www.wunderground.com.

3.3. Keeling-plot analysis

CO_2 and CH_4 parameters (concentrations and $\delta^{13}C$ values) were analyzed according to the Keeling plot analysis (Keeling, 1958, 1961), to recognize the main sources of these gases. The method relies on a two end-member mixing model, i.e. the environmental background and local source(s), and is based on two mass balance equations (Pataki et al., 2003; Venturi et al., 2020):

i) $C_m = C_b + C_s$

ii) $\delta^{13}C_m \times C_m = \delta^{13}C_b \times C_b + \delta^{13}C_s \times C_s$

where C and $\delta^{13}C$ are the concentration and the carbon isotopic composition of the gaseous species respectively, and *m*, *b* and *s* subscripts refer to the measured, background and source(s) values respectively. By combining equations (i) and (ii) as follows (iii), a straight line is identified on a 1/C vs. $\delta^{13}C$ plot, whose intercept corresponds to the isotopic signature of the emitting source:

iii) $\delta^{13}C_m = \frac{(\delta^{13}C_b - \delta^{13}C_s) \times C_b}{C_m} + \delta^{13}C_s$

When the gas concentration increases, the isotopic ratios tend to move away from the background values as a function of the source(s) characteristics. The background values can remain unknown, but both the background and source(s) values are assumed to be constant during the observation period (Pataki et al., 2003; Venturi et al., 2020).

Considering the prerequisite of constant mixing of background and sources, we applied the Keeling plot analysis to short-time intervals (≤6 h) at each site, having pre-processed data in 5min-moving averages, which allowed improvement of the stability in data trends, attenuating the oscillations due to sudden gusts of wind. Data reduction (minute-averages and moving averages) were performed using R (R Core Team, 2017) implemented with the Openair package (Carslaw and Ropkins, 2012; Carslaw, 2014). The linear regression was performed using the ordinary least squares (OLS) method, as recommended in Zobitz et al. (2006).

The R^2 determination coefficient was used to verify the ability of the linear regression model to describe the data distribution. The estimated isotopic signature of the source is not to be considered reliable when $R^2 < 0.75$.

4. Results

The summary descriptive statistical parameters (minimum, maximum, mean, standard deviation) on the minute-averaged data measured at each site, and meteorological parameters (wind direction, wind speed), are reported in Table 1.

4.1. Meteorological parameters

During the first campaign of measurements, the weather was mainly fair. On January 21, 2020, prevailing wind direction blew from NE-NNE in the late afternoon, with wind speed around 13 km/h, and from N-NW sector during nighttime, with lower wind speed (5–11 km/h) (Table 1). On January 22, 2020, prevailing wind directions blew from N-NNE in the early morning, while during the late morning, the afternoon and nighttime they were mostly variable with a speed constantly <8 km/h (Table 1). On January 23, 2020, wind speed was relatively low (3–5 km/h), mostly from N-NE (Table 1).

During the second campaign, the weather conditions were partially cloudy or cloudy. On the afternoon of June 9, 2020, wind blew mainly from W, with wind speed ranging from 19 to 22 km/h (Table 1). In the morning and afternoon of June 10, 2020, wind direction blew mainly from W with wind speed from 11 to 24 km/h (Table 1). Eventually, on the morning of June 11, 2020, prevailing wind direction came from SSW-SW, with wind speed from 11 to 19 km/h (Table 1).

Air temperature was higher in June (19–23 °C) than in January 2020 (3–15 °C). During both the observation periods, it followed a typical diurnal cycle, characterized by maximum values at early afternoon and minimum at nighttime and early morning.

Air humidity was higher in January (minimum 48%, maximum 100%) than in June 2020 (minimum 34%, maximum 73%), and reached the highest values during nighttime and the lowest ones at midday.

4.2. Concentrations and $\delta^{13}C$ values of CO_2 and CH_4

4.2.1. CO_2

The measurement sites located near the main fumaroles (FU), the cemented conduit at the entrance of the sport center (AC) and the new geothermal well (GW) displayed relatively high CO_2 concentrations, ranging from 922 to 1,677, from 746 to 1,197, and from 774 to 1,061 mg/m^3, respectively (Table 1), whereas the $\delta^{13}C$–CO_2 values were from −10.5 to −5.9, from −10.3 to −6.8, and from −8.0 to −5.7‰ vs. V-PDB, respectively (Table 1). At FU, the mean values of CO_2 concentrations and $\delta^{13}C$–CO_2 were 1,090 mg/m^3 (SD: 120; Table 1) and −8.6‰ vs. V-PDB (SD: 0.9), respectively. At the AC site, CO_2 concentrations were on average higher in January 2020 (mean: 980 mg/m^3, SD: 107; Table 1) than in June 2020 (mean: 831 mg/m^3, SD: 77; Table 1), whereas the average $\delta^{13}C$–CO_2 values in January 2020 (mean: −8.9‰ vs. V-PDB, SD: 0.7; Table 1) and in June 2020 (mean: −8.4‰ vs. V-PDB, SD: 0.6; Table 1) were similar. At GW site, the mean values of CO_2 concentrations and $\delta^{13}C$–CO_2 were, respectively, as follows: 884 mg/m^3 (SD: 53; Table 1), and −7.0‰ vs. V-PDB (SD: 0.4; Table 1) in the morning of June 10, 2020; 871 and mg/m^3 (SD: 66; Table 1), and −6.9 and ‰ vs. V-PDB (SD: 0.5; Table 1) in the afternoon of June 10, 2020; 864 and mg/m^3 (SD: 55; Table 1) and −7.2‰ vs. V-PDB (SD: 0.4; Table 1) on June 11, 2020. CO_2 concentrations and isotopic values showed a direct correlation in all the three sites (Fig. A.1-6).

Surprisingly, the highest CO_2 concentrations were measured at the distal HT site, where they ranged from 1,087 to 2,109 mg/m^3 on January 21-22, 2020, (mean: 1,567 mg/m^3, SD: 230; Table 1), and from 1,170 to 2,193 mg/m^3 on January 22-23, 2020, (mean: 1,591 mg/m^3, SD: 154; Table 1). The $\delta^{13}C$–CO_2 values ranged from −12.4 to −5.8‰ vs. V-PDB on January 21-22, 2020, (mean: −7.6‰ vs. V-PDB, SD: 1.5; Table 1), and from −11.4 to −5.7‰ vs. V-PDB on January 22-23, 2020, (mean: −7.3‰ vs. V-PDB, SD: 1.0; Table 1). Similarly to the previous sites, CO_2 concentrations and isotopic values were directly correlated

(Fig. A.7 and A.8). During both the measurement sessions carried out at this site, the CO_2 concentrations (and the associated isotopic values) were significantly higher at nighttime than in the morning (Fig. A.7 and A.8). Relatively high CO_2 concentrations (from 998 to 1,374 mg/m^3, mean: 1,176 mg/m^3, SD: 110; Table 1) were also measured at the other distal site (DS), where the $\delta^{13}C$–CO_2 values ranged between −14.3 and −12.5‰ vs. V-PDB (mean: −13.6‰ vs. V-PDB, SD: 0.4; Table 1). Notably, in this case CO_2 concentrations and $\delta^{13}C$–CO_2 values were inversely correlated (Fig. A.9).

4.2.2. CH_4

During the period of observation, the CH_4 concentrations measured at the FU site showed minor variations (from 1.41 to 1.46 mg/m^3; Table 1) around the mean value of 1.43 mg/m^3 (SD 0.009; Table 1) (Fig. A.10). At AC, CH_4 concentrations ranged from 1.26 to 1.40 mg/m^3 and were on average higher in January 2020 (mean: 1.40 mg/m^3, SD: 0.003; Table 1) than in June 2020, when the mean CH_4 concentration value was 1.27 mg/m^3 (SD: 0.002; Table 1) (Fig. A.11 and A.12). The GW site displayed almost constant CH_4 concentrations during the three measuring sessions (average values: 1.30 mg/m^3; Table 1), ranging from 1.29 to 1.33 mg/m^3 (SDs: 0.003 and 0.005 on June 10, 2020, and 0.004 on June 11, 2020; Table 1) (Fig. A.13-15). Overall, CH_4 concentrations at sites near hydrothermal discharges were lower in June (i.e. at AC and GW sites) than in January (i.e. FU and AC sites).

At the HT site, CH_4 showed almost constant concentrations during nighttime, with mean values of 1.45 mg/m^3 (SD: 0.05; Table 1) on January 21-22, 2020, and 1.42 mg/m^3 (SD: 0.05; Table 1) on January 22-23, 2020, whereas increasing trends occurred in the morning, from 1.43 to 1.63 mg/m^3 and from 1.40 to 1.53 mg/m^3, respectively (Fig. A.16 and A.17). It is worth noting that the highest CH_4 concentration (1.72 mg/m^3), measured at 3:35 on January 23, 2020 (Fig. A.17), corresponds to an abrupt decrease in CO_2 concentrations (Fig. A.8). At DS site, the CH_4 concentrations ranged from 1.54 to 2.23 mg/m^3, with a mean value of 1.69 mg/m^3 (SD: 0.14; Table 1).

The $\delta^{13}C$–CH_4 values varied over a relatively narrow range among the measuring sites. At FU, the $\delta^{13}C$–CH_4 ranged from −49.8 to −43.8‰ vs. V-PDB (mean: −45.9‰ vs. V-PDB, SD: 0.88; Table 1). At AC site, $\delta^{13}C$–CH_4 values varied from −49.3 to −44.7‰ vs. V-PDB in January 2020 (Table 1), and from −52.8 to −48.5‰ vs. V-PDB in June 2020 (Table 1), showing on average more negative values in spring (mean: −50.8‰ vs. V-PDB, SD: 0.88; Table 1) than in winter (mean: −47.0‰ vs. V-PDB, SD: 0.75; Table 1). The $\delta^{13}C$–CH_4 values measured on June 10 (morning and afternoon) and 11, 2020, at GW site ranged from −51.2 to −45.0‰ vs. V-PDB, from −48.7 to −44.1‰ vs. V-PDB and from −48.8 to −45.4‰ vs. V-PDB, respectively (mean: −48.6, −46.6, and −47.0‰ vs. V-PDB, respectively; and SD: 1.17, 0.94, and 0.84, respectively; Table 1). At the HT site, the $\delta^{13}C$–CH_4 values ranged from −50.4 to −44.2‰ vs. V-PDB on January 21-22, 2020 (mean: −46.3‰ vs. V-PDB, SD: 0.85; Table 1), and from −50.0 to −45.2‰ vs. V-PDB on January 22-23, 2020 (mean: −47.1‰ vs. V-PDB, SD: 0.78 Table 1). The DS site showed $\delta^{13}C$–CH_4 values from −49.9 to −44.8‰ vs. V-PDB (Table 1), with a mean value of −47.8‰ vs. V-PDB (SD: 1.10; Table 1). Differently from CO_2, no clear correlation was observed between CH_4 concentrations and $\delta^{13}C$–CH_4 values.

4.3. Concentrations of H_2S and SO_2

The concentrations of H_2S and SO_2 at the FU site ranged from 94 to 1,333 μg/m^3 (mean: 362 μg/m^3, SD: 184; Table 1) and from 7.05 to 44 μg/m^3 (mean: 20 μg/m^3, SD: 7.3; Table 1), respectively, and showed a positive correlation (Fig. A.19). Significantly lower H_2S and SO_2 concentrations were measured at the AC site both in January 2020 (from 0.78 to 82 μg/m^3 and from 1.30 to 9.79 μg/m^3, respectively) and in June 2020 (from 1.40 μg/m^3 to 396 μg/m^3 and from 3.26 to 29 μg/m^3, respectively) (Table 1; Fig. A.20 and A.21). The average concentrations of both S-bearing species were less abundant in winter (H_2S and SO_2 mean: 10 and 4.58 μg/m^3 respectively, H_2S and SO_2 SD: 12 and 1.7 respectively; Table 1) than in spring (H_2S and SO_2 mean: 45 and 10 μg/m^3 respectively, H_2S and SO_2 SD: 68 and 5.4 respectively; Table 1). The highest H_2S concentrations were measured at the GW site (Fig. A.22-24), where they ranged from 2.28 to 1,570 μg/m^3 (Table 1), whereas SO_2 concentrations were from 9.10 to 87 μg/m^3 (Table 1). The mean H_2S concentrations values were, 497 μg/m^3 in the morning of June 10, 2020 (SD: 188; Table 1), 375 μg/m^3 in the afternoon of June 10, 2020 (SD: 254; Table 1), and 233 μg/m^3 on June 11, 2020 (SD: 198; Table 1), whereas the mean values of SO_2 concentrations were 42 μg/m^3 (SD: 10.6; Table 1), 37 μg/m^3 (SD: 15.5; Table 1), and 20 μg/m^3 (SD: 8.6; Table 1), respectively.

At the HT site, H_2S concentrations varied from 10 to 618 μg/m^3 on January 21-22, 2020 (mean: 192 μg/m^3, SD: 126; Table 1), and from 5.83 to 126 μg/m^3 on January 22-23, 2020 (mean: 44 μg/m^3, SD: 29; Table 1), whereas SO_2 concentrations were from 0.54 to 21 μg/m^3 on January 21-22, 2020 (mean: 9.15 μg/m^3, SD: 4.2; Table 1), and ≤11 μg/m^3 on January 22-23, 2020 (mean: 4.50 μg/m^3, SD: 1.9; Table 1). During the first measurement night, H_2S and SO_2 concentrations were relatively high, showing a positive correlation (except at lower H_2S values; Fig. A.25). The DS site was characterized by H_2S and SO_2 concentrations ranging from 27 to 91 μg/m^3 and from 11 to 92 μg/m^3 (Table 1), with mean concentration values of 52 μg/m^3 for H_2S (SD: 16; Table 1) and 23 μg/m^3 for SO_2 (SD: 15; Table 1), and showed an inverse correlation (Fig. A.27).

5. Discussion

5.1. Hydrothermal gas input in the air

In order to investigate the distribution and behavior of the hydrothermal gases in the air, as well as their possible use as tracers to distinguish natural and anthropogenic sources in environments where human settlements and hydrothermal fluid discharges coexist, we firstly analyzed the chemical and isotopic data measured in air from sites located near to the main hydrothermal discharges.

Excluding water vapor, CO_2 and H_2S are the main volatile species commonly emitted by hydrothermal systems (Carapezza et al., 1984, 2003; Caliro et al., 2007; Granieri et al., 2009; Viveiros et al., 2010; Cabassi et al., 2017). CO_2 is also emitted in the air from several other natural sources (mainly vegetation and oceans; Carlson et al., 2001; Riebeek and Simmon, 2011), and most anthropic activities related to the massive exploitation and combustion of fossil fuels (Venturi et al., 2019, 2020), resulting in global air background concentrations up to 730 mg/m^3 [1] (NOAA/ESRL Global Monitoring Division; www.esrl.noaa.gov/gmd; Table 3), which basically represent the "background air" value. H_2S is naturally produced in wetlands and stagnant water under reducing conditions (Rubright et al., 2017 and references therein), and by different human activities, e.g. pulp and paper mills, rayon textile manufacturing, chemical manufacturing, waste disposal (Llavador Colomer et al., 2012), extraction and refining of oil and natural gas, production of geothermal energy (WHO, 1981, 2000a, 2003; NYS Department of Health, 2005; Thorsteinsson et al., 2013; Rubright et al., 2017). Hence, in those sites of the study area located in the proximity of the hydrothermal discharges (FU, GW and AC; Fig. 1b), the measured CO_2 was derived from both the hydrothermal contributions and a large list of undefined anthropogenic sources, whereas no significant H_2S sources, other than the hydrothermal discharges, can be recognized. In agreement with these considerations, the H_2S/CO_2 ratios measured at FU and GW strongly increased with the H_2S concentrations, approaching those of gases directly collected from the corresponding hydrothermal discharges, i.e. Pisciarelli fumarole (Caliro et al., 2007) and the geothermal well (INGV-OV, 2020) (Fig. 2a), although the discharged

[1] Conversion factors: 1 ppm CO_2(20°C, 101.325 kPa) ≈ 1.83mg/m^3 CO_2
1 mg/m^3 CO_2 ≈ 0.55ppm CO_2.

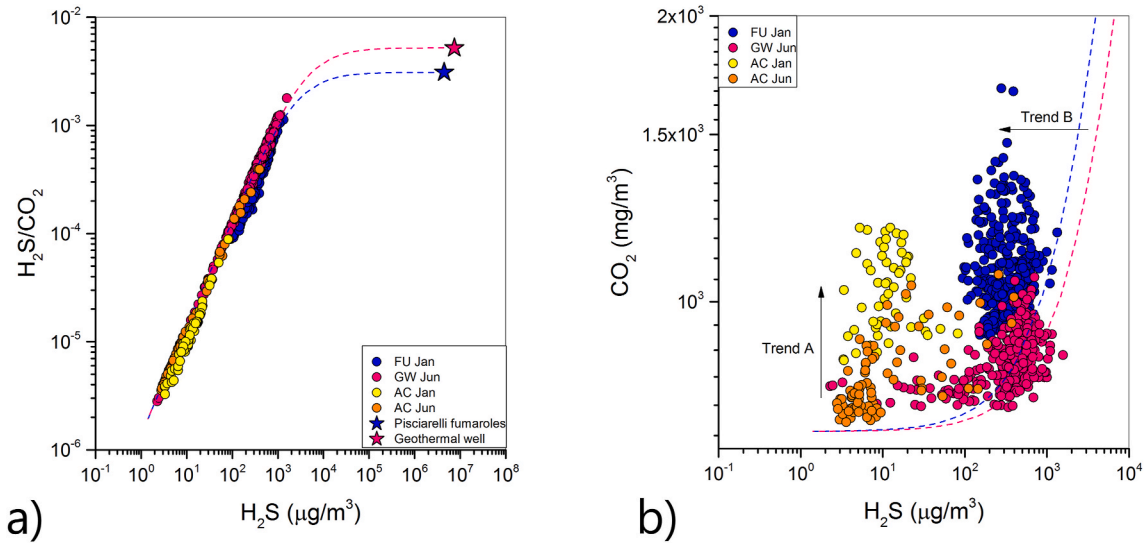

Fig. 2. (a) H_2S/CO_2 vs. H_2S binary diagram of FU (blue dots), GW (magenta dots), and AC (yellow and orange dots) sites. Hydrothermal discharges of Pisciarelli fumaroles (blue star) and the geothermal well (magenta stars) are also reported. The mixing lines between (i) hydrothermal components, and (ii) air, are shown as dashed lines. (b) CO_2 vs. H_2S binary diagram of FU (blue dots), GW (magenta dots), and AC (yellow and orange dots) sites. The mixing lines between (i) hydrothermal components, and (ii) air, are reported as abovementioned. The black arrows show trends of (i) enrichment in CO_2 (Trend A), and (ii) depletion in H_2S (Trend B). (For interpretation of the references to colour in this figure legend, the reader is referred to the Web version of this article).

hydrothermal gases were strongly diluted (up to 3 orders of magnitude) at the FU and GW measurement stations. On the other hand, as the H_2S concentrations decreased, the H_2S/CO_2 ratio decreased, according to a distribution basically controlled only by dilution with the local background (Fig. 2a). However, in the H_2S vs. CO_2 binary diagram (Fig. 2b), the FU and GW data display a significant CO_2-enrichment with respect to the dilution curves (blue and magenta dashed lines), suggesting (i) a local heterogeneity of background CO_2 (trend A) likely due to anthropogenic inputs from the urban area, and (ii) a partial H_2S depletion (trend B) possibly caused by oxidizing processes typically affecting this gas compound in air, as observed by Badalamenti et al. (2001) and Carapezza et al. (2003) based on measurement of air composition in other areas affected by hydrothermal emissions. Both the H_2S concentrations and H_2S/CO_2 ratios measured at AC were on average lower than those measured at the other two proximal sites (FU and GW). As a first approximation, this could be ascribed to the relatively long distance separating AC and the Pisciarelli fumarole (Fig. 1b) and/or to the occurrence of anthropogenic inputs of CO_2 affecting the AC background value (Fig. 2b; trend A). However, it has to be considered that the measurements at the AC site were likely influenced by gas emissions from the cemented conduit located just few meters away (Fig. 1b). Gases from this source were likely depleted in H_2S, being fed by emissions at the periphery of the Pisciarelli main emitting site, where the shallow aquifer has a relatively high pH. This hypothesis is confirmed by the distribution of the AC measurements in the CO_2 vs. H_2S binary diagram (Fig. 2b; trend B), showing relatively low H_2S concentrations at CO_2 values comparable to those measured at FU and GW. Noteworthy, part of the AC samples plot at intermediate position between the AC main group and the FU samples, particularly in June (Fig. 2b), suggesting occasional contributions from the Pisciarelli fumaroles related to more favorable wind conditions.

By applying the Keeling plot analysis (Keeling, 1958, 1961) to the CO_2 concentrations in air measured at the FU site (Fig. 3a), assuming a two-member mixing model between background air and hydrothermal gases, the isotopic signature of CO_2 discharged from the Pisciarelli fumaroles was estimated at -0.4 ± 0.21‰ vs. V-PDB ($R^2 = 0.82$; Table 2).

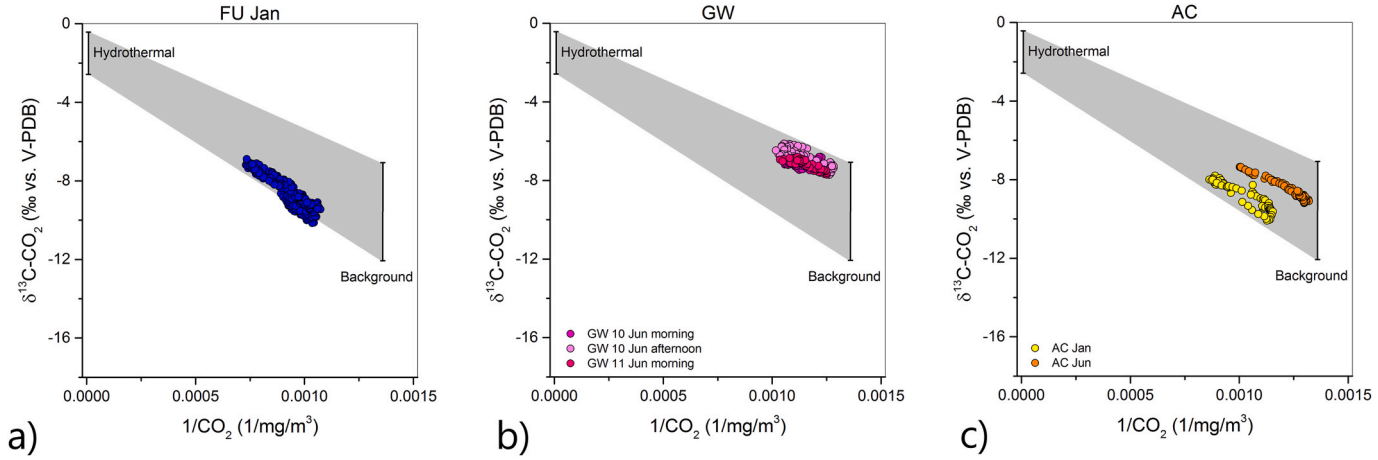

Fig. 3. Keeling plot of $\delta^{13}C$–CO_2 vs. $1/CO_2$ of (a) FU, (b) GW, and (c) AC. The mixing between (i) hydrothermal discharges, and (ii) local background, is depicted with the grey area. The isotopic ranges of hydrothermal and background end-members are also reported (black lines). See text for more details. (For interpretation of the references to colour in this figure legend, the reader is referred to the Web version of this article).

Table 2
$\delta^{13}C–CO_2$ and $\delta^{13}C–CH_4$ (‰ vs. V-PDB) source values extrapolated using the Keeling plot analysis. Standard errors and determination coefficients R^2 are also reported.

Site		$\delta^{13}C–CO_2$	Standard error	R^2	$\delta^{13}C–CH_4$	Standard error	R^2
FU	January 22, 2020	−0.4	0.21	0.82			
AC	January 21, 2020	−2.8	0.29	0.85			
	June 09, 2020	−1.8	0.16	0.95			
GW	June 10, 2020 (morning)			<0.75			
	June 10, 2020 (afternoon)			<0.75			
	June 11, 2020	−2.5	0.3	0.78			
HT	January 21–22 (night)	−2.9	0.06	0.93			
	January 21–22 (morning)				−60.3	0.6	0.70
	January 22–23 (night)			<0.75			<0.75
	January 22–23 (morning)						<0.75
DS	January 23, 2020			<0.75			<0.75

As expected, this value is consistent with those reported in literature (e.g. Caliro et al., 2007) for fumarolic CO_2 of the Pisciarelli area. According to a similar approach (Fig. 3b), the $\delta^{13}C–CO_2$ estimates based on the data acquired at the GW site on June 11 (when winds were blowing from SSW-SW, i.e. the measurement equipment was upwind to the geothermal well; Fig. 1b) allowed to confirm the hydrothermal origin of the fluids emitted by the geothermal well under construction (−2.5 ± 0.30‰ vs V-PDB, $R^2 = 0.78$; Table 2). On the contrary, on June 10 the coefficients of determination R^2 were too low (<0.75; Table 2) to determine with certainty the isotopic signature of the CO_2 source. This might indicate that, notwithstanding the proximity to the hydrothermal fluid source (40 m, Fig. 1b), the area was affected by anthropogenic CO_2 input, controlled by variable weather conditions, producing a large dispersal of data. The $\delta^{13}C–CO_2$ values computed using the data measured at the AC site (Fig. 3c) were −2.8 ± 0.29‰ vs V-PDB ($R^2 = 0.85$) and −1.8 ± 0.16‰ vs. V-PDB ($R^2 = 0.95$) (Table 2) in January and June, respectively. The slight difference between the $\delta^{13}C–CO_2$ values computed for the FU and AC sites was possibly due to a more negative isotopic signature of the CO_2 emitted from the cemented conduit, likely influencing the AC site, since this gas interacted with the surficial aquifer occurring at the periphery of the Pisciarelli fumarolic area.

5.2. SO_2 and CH_4

In urban environments, SO_2 originates from several anthropogenic activities, mainly related to the combustion of fossil fuels containing sulfur (WHO, 2000b). Accordingly, the natural SO_2 background value in urban and industrial zones is up to 25 μg/m^3, whereas in rural areas it is generally <5 μg/m^3 (WHO, 2000b, Table 3). Fluids emitted from hydrothermal emissions are generally characterized by extremely low SO_2 concentrations with respect to those of H_2S, which is the most stable S-bearing gas compound at the highly reducing redox conditions typically dominating the hydrothermal reservoirs (e.g. Giggenbach, 1996). The time-plots of the H_2S and SO_2 concentrations measured at the FU, GW and AC sites (Fig. A.19-24), show that, at relatively high H_2S concentrations (>100 μg/m^3), H_2S and SO_2 have almost identical trends, suggesting that the peaks of SO_2 in air were significantly related to inputs from the hydrothermal emissions, being likely produced by oxidation of hydrothermal H_2S since primary hydrothermal SO_2 is to be considered negligible. Differently, when the hydrothermal gas fraction in air was too low, SO_2 produced from H_2S was masked by that from different, likely anthropogenic, sources.

Although CH_4 is by far the most abundant organic volatile in hydrothermal-volcanic fluids (e.g. Giggenbach, 1996), the concentrations of this gas in the fumarolic fluids is relatively low (about 7 mg/m^3; Caliro et al., 2007, Table 3). In agreement with the dilution magnitude observed for CO_2 and H_2S (Fig. 2a), the hydrothermal contribution to the CH_4 concentrations in FU, GW and AC sites would range from 0.007 to 0.7 mg/m^3. However, is likely to assume that part of the CH_4 discharged from the hydrothermal vents was lost by oxidation in the air (e.g. Holmes, 2018). This explains the lack of any evidence of hydrothermal CH_4 contribution, as shown by the CH_4 concentrations measured in air close to the hydrothermal discharges, which were constantly <1.50 mg/m^3 (Table 1) and did not display a correlation with the trends of the typical hydrothermal species (Fig. A.10-15). The latter value slightly exceeds that of global background (1.26 mg/m^3; Dlugokencky, 2021, Table 3), as commonly observed in urban areas (e.g. Lowry et al., 2001; Chamberlain et al., 2016; Venturi et al., 2020, 2021), where different anthropogenic CH_4 sources, e.g. domestic heating, vehicular traffic and landfills (e.g. Zazzeri et al., 2017), and natural inputs, including wetlands and green areas (e.g. Bartlett and Harriss, 1993; Saunois et al., 2019), likely occur.

5.3. Insights from distal sites

The spatial distribution of the fluids emitted in the air from the hydrothermal discharges at increasing distance from the Pisciarelli hydrothermal field (i.e. at the HT and DS sites; Fig. 1b) was investigated to evaluate the impact of the hydrothermal emissions on the air quality of inhabited areas and their possible use as tracers to distinguish natural (hydrothermal) and anthropogenic sources.

As mentioned above, H_2S in the investigated area is to be considered purely of hydrothermal origin, whilst CH_4 was related to the local background, with no evidence of the influence of the hydrothermal gas discharges even near the main fumarolic vents. In agreement with these considerations, the concentrations in air of these two gas species, plotted in the H_2S vs. CH_4 binary diagram (Fig. 4a), were clearly independent. In fact, while the lowest CH_4 concentrations were found at those sites close to Pisciarelli, relatively high CH_4 values were measured at DS (i.e. the measurement site located at the highest distance from the fumaroles) and at HT, with no relation with the H_2S concentrations. It is worth noting that the CH_4 background values measured in winter data (FU, AC Jan, HT and DS) were significantly higher than those measured in June (AC Jun and GW) (Fig. 4a). This is possibly related to the higher anthropogenic contribution to CH_4 emissions during the colder season due to the use of the domestic heating, as commonly observed in urban

Table 3
Chemical (CO_2, H_2S, CH_4 and SO_2) and isotopic ($\delta^{13}C–CO_2$ and $\delta^{13}C–CH_4$) composition of the Pisciarelli fumarole (Caliro et al., 2007), the geothermal well (INGV-OV, 2020) and atmosphere (Quay et al., 1999; WHO, 200a, 200 b; NOAA/ESRL Global Monitoring Division; www.esrl.noaa.gov/gmd).

	H_2O (mg/m^3)	CO_2 (mg/m^3)	H_2S (μg/m^3)	CH_4 (mg/m^3)	SO_2 (μg/m^3)	$\delta^{13}C–CO_2$ (‰ vs. V-PDB)	$\delta^{13}C–CH_4$ (‰ vs. V-PDB)
Pisciarelli	5,03,020	2,13,097	6,59,780	6.7	u.d.l.	−2.9	−22.1
Geothermal well	5,43,003	1,15,722	6,02,844	6.8	u.d.l.	−1.2	
Atmosphere		730	0.3	1.26	<5	−8.0	−47.4

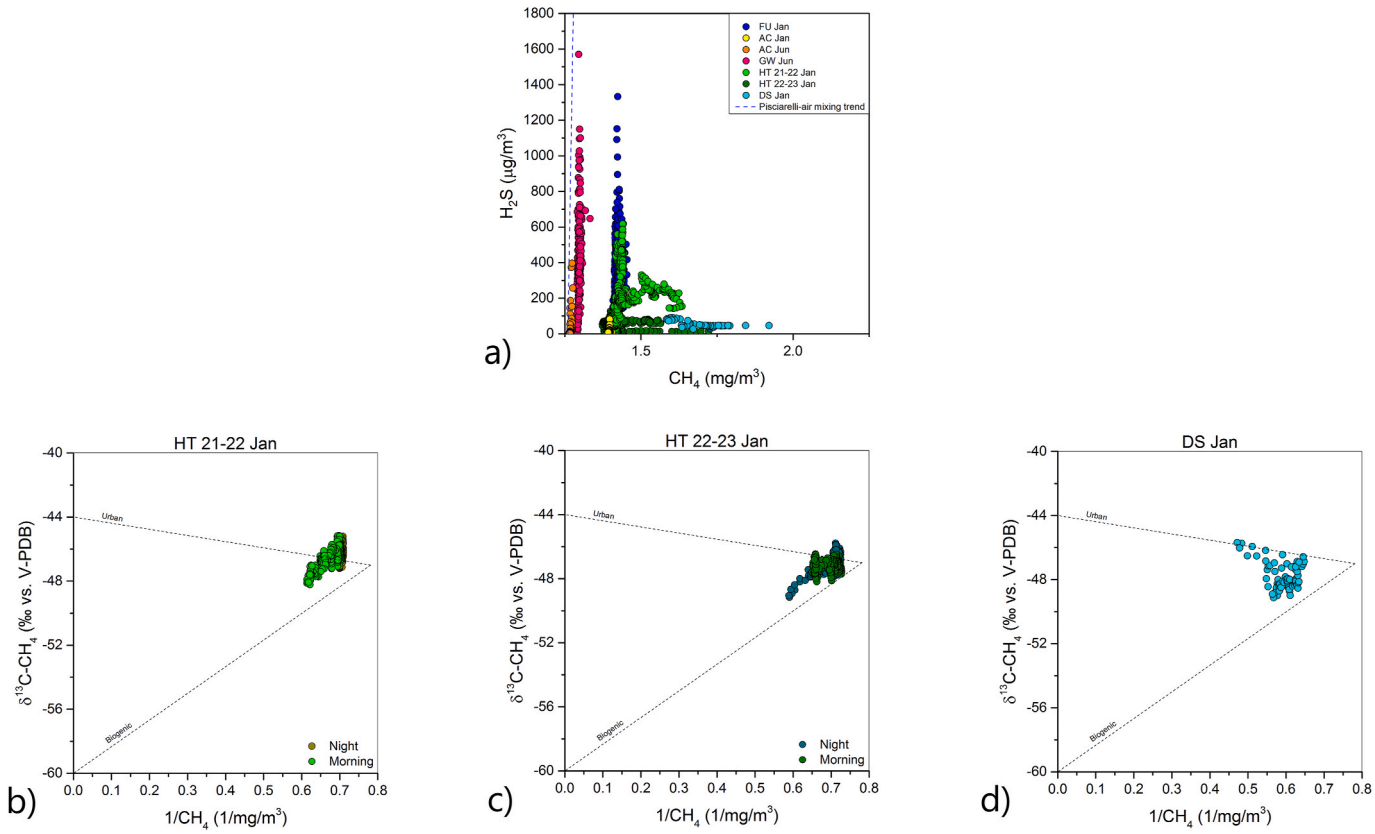

Fig. 4. (a) H_2S vs. CH_4 binary diagram of FU (blue dots), AC (yellow and orange dots), GW (magenta dots), HT (light and dark green dots), and DS (turquoise dots). The mixing trend between air and the Pisciarelli fumarole is also reported (blue dashed line) (b) Keeling plot of $\delta^{13}C$–CH_4 vs. $1/CH_4$ of HT during 21st-22nd January 2020 nighttime measurements. The data are divided into night data (0:00–5:59; olive green dots) and morning data (6:00-end of measurements; light green dots). (c) Keeling plot of $\delta^{13}C$–CH_4 vs. $1/CH_4$ of HT during 22nd-23rd January 2020 nighttime measurements. The data are divided into night data (0:00–5:59; teal green dots) and morning data (6:00-end of measurements; dark green dots). (d) Keeling plot of $\delta^{13}C$–CH_4 vs. $1/CH_4$ of DS (turquoise dots). In (b), (c) and (d), the mixing trends between (i) air background and urban emissions, and (ii) air background and biogenic emissions, are reported (black dashed lines). (For interpretation of the references to colour in this figure legend, the reader is referred to the Web version of this article).

areas (Venturi et al., 2020, 2021 and references therein).

Contrary to the sites close to Pisciarelli, where CH_4 concentrations were not sufficient to extrapolate information on the isotopic characteristics of the emissive source through the Keeling plot analysis, at HT and DS sites the CH_4 concentrations reached values sufficiently high to apply this statistical approach (Fig. 4b–d). Considering the prerequisite of constant mixing of background (assumed as atmospheric CH_4, i.e. 1.26 mg/m^3 [2] and −47.4‰ vs. V-PDB; Table 3) (Dlugokencky, 2021; Quay et al., 1999) and sources, data measured at HT site, respectively, during night (0:00–5:59) and morning (6:00-end of detection) were distinguished (Fig. 3b and c). As depicted in the Keeling plot of $\delta^{13}C$–CH_4 vs. $1/CH_4$ (Fig. 4b), at HT the concentrations and $\delta^{13}C$ values of CH_4 were relatively constant during nighttime on January 21-22 (around 1.45 mg/m^3 and −46.3‰ vs. V-PDB, respectively; Table 1), pointing to the absence of relevant local emitting sources. In the morning, the increase of the CH_4 concentrations (up to 1.64 mg/m^3; Table 1) was coupled with a decrease in $\delta^{13}C$–CH_4 down to −50.1‰ vs. V-PDB (Table 1). According to the Keeling plot analysis computed on the morning data, the intercept was at −60.3 ± 0.6‰ vs. V-PDB (Fig. 4b; Table 2), corresponding to $\delta^{13}C$–CH_4 values typical of biogenic sources, including landfills (around −58‰ vs. V-PDB; e.g. Zazzeri et al., 2017), agriculture- and livestock-related emissions (from −66 to −55‰ vs. V-PDB; e.g. Levin et al., 1993; Lowry et al., 2001; Townsend-Small et al., 2012; Zazzeri et al., 2017 and references therein), emissions from wastewater treatments (around −53‰ vs. V-PDB; e.g. Zazzeri et al., 2017) and wetlands (around −60‰ vs. V-PDB; e.g. Quay et al., 1988, 1999). Although the relatively low correlation coefficient of the alignment depicted by the HT morning data (R^2 = 0.70; Table 2) suggests caution to evaluate the computed isotopic signature of the CH_4 source affecting this site, it is reliable to suppose that it was mostly related gas vapors released from the wastewater tank hosted in the parking lot of the hotel (Fig. 1b). The Keeling plot of $\delta^{13}C$–CH_4 vs. $1/CH_4$ of the measurements carried out at the HT site on January 22-23 (Fig. 4c) shows a similar distribution with that computed with the data measured the previous day (Fig. 4b), confirming the occurrence of a local biogenic CH_4 source at the HT site. In the Keeling plot of $\delta^{13}C$–CH_4 vs. $1/CH_4$ of the DS site (Fig. 4d), which as aforementioned displayed the highest concentrations of CH_4 (up to 2.23 mg/m^3; Table 1), data distribution seems to be consistent with a CH_4 source having relatively high $\delta^{13}C$–CH_4 value. Such an isotopic signature, i.e. about −44‰ vs. V-PDB (Fig. 4d), is consistent with that of a number of urban CH_4 sources including natural gas employment (e.g. Schwietzke et al., 2016; Sherwood et al., 2017; Venturi et al., 2020, 2021 and references therein).

Notwithstanding the distance separating HT from the hydrothermal discharges of Pisciarelli, the highest concentrations of CO_2 were observed at this site (up to 2,193 mg/m^3; Table 1), possibly due to the static conditions of the near-surface atmosphere during nighttime and to the concave morphology of the parking lot (Fig. 1b). As depicted in the Keeling plot of $\delta^{13}C$–CO_2 vs. $1/CO_2$ (Fig. 5a), the CO_2 at HT showed isotopic characteristics that indissolubly bound it to a hydrothermal origin (−2.9 ± 0.06‰ vs. V-PDB, R^2 = 0.93; Table 2), even if it was

[2] Conversion factors : 1 ppm CH_4(20°C, 101.325 kPa) ≈ 0.67mg/m^3 CH_4
1 mg/m^3 CH_4 ≈ 1.5 ppm CH_4.

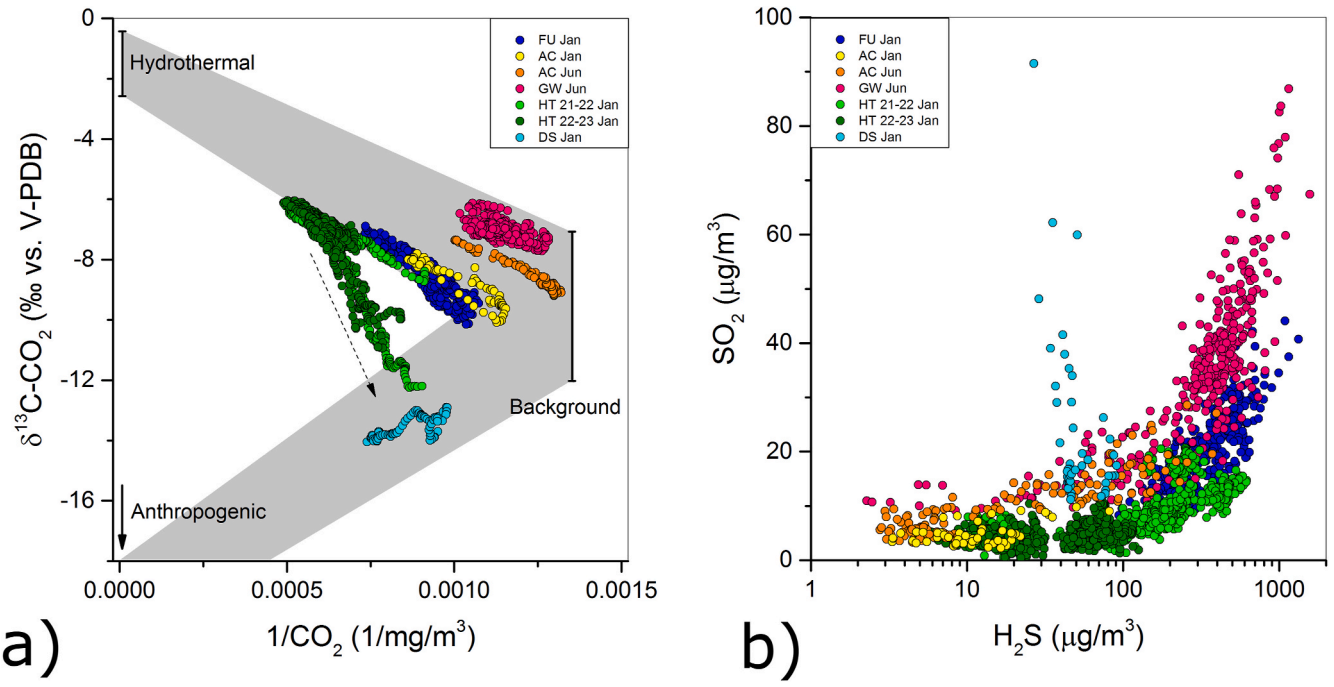

Fig. 5. (a) Keeling plot of $\delta^{13}C$–CO_2 vs. $1/CO_2$ of FU (blue dots), AC (yellow and orange dots), GW (magenta dots), HT (light and dark green dots), and DS (turquoise dots). The isotopic ranges of hydrothermal, background and anthropogenic end-members are reported (black lines). The mixing between (i) hydrothermal discharges and local background, and (ii) anthropogenic emissions and local background, are depicted with the grey areas. The shift of a branch of HT data toward the DS site field is marked with the black dashed arrow. (b) SO_2 vs. H_2S binary diagram of FU (blue dots), AC (yellow and orange dots), GW (magenta dots), HT (light and dark green dots), and DS (turquoise dots). (For interpretation of the references to colour in this figure legend, the reader is referred to the Web version of this article).

affected by mixing with the atmospheric background. However, the HT site was also affected by CO_2 inputs from anthropogenic sources, possibly related, as for CH_4, to the wastewater tank emissions and other local biogenic sources, which, consisting of lower CO_2 concentrations and more negative values of $\delta^{13}C$–CO_2, shifted a branch of data toward the DS site field (Fig. 5a dashed arrow). The latter is the only site where emitted CO_2, characterized by relatively low $\delta^{13}C$–CO_2 values independently on CO_2 concentrations (Fig. 5a), can be purely ascribe to anthropogenic sources related to the urban environment (e.g. Chamberlain et al., 2016; Venturi et al., 2020 and references therein).

In summary, the detected CO_2 in the study area resulted from the mixing, at different proportions, between three main endmembers: (i) the hydrothermal discharges, (ii) anthropogenic emissions and (iii) the local atmospheric background. The latter displayed a relatively wide range of isotopic values (Fig. 5a), possibly due to the variable direction of prevailing winds, which came from the N-E sector (i.e. from the hinterland and cities sector) in January, matching the lowest isotopic values (Fig. 5a), and from the S–W sector (i.e. from the Solfatara-Pisciarelli hydrothermal area and the sea sector) in June, when the highest background isotopic values were measured (Fig. 5a).

The aforementioned hypothesis of partial oxidation of the hydrothermal H_2S in the air to produce SO_2, is confirmed by the distribution of data in the SO_2 vs. H_2S binary diagram (Fig. 5b), which provides strong evidence for the (genetic) relationship between the two S-bearing gases. Data measured at the GE site were not consistent with the main trend, being SO_2 inversely correlated with H_2S (Fig. 5b). This suggests that the origin of SO_2 measured at this distal site was mainly anthropogenic, i.e. related to the crowded urban settlements and the intense vehicular traffic characterizing this zone.

6. Conclusions

Hydrothermal areas are largely recognized as hot spots of pollutant emissions, thus representing an environmental hazard in the near-surface atmosphere (e.g. Carapezza et al., 1984, 2003; Badalamenti et al., 2001; Vaselli et al., 2011; Tassi et al., 2009, 2013, 2015; Aiuppa, 2015; Cabassi et al., 2017). This study, based on a geochemical survey of air quality in the proximity of Pisciarelli, i.e. one of the main hydrothermal emissions at Campi Flegrei, evidenced the occurrence of anomalously high CO_2 and H_2S concentrations at the near-surface level, clearly related to the hydrothermal discharges, as confirmed by the isotopic signature of CO_2 measured at sites located at a distance <325 m from the main hydrothermal emission area (FU, AC, GW and HT). H_2S measured in these sites is considered purely of hydrothermal origin, being the most abundant sulfur compound in hydrothermal gases and in absence of significant H_2S anthropogenic sources. At HT, secondary anthropogenic CO_2 sources were also recognized, likely related to vapors released from a wastewater system hosted in the parking lot of the hotel. This hypothesis was confirmed by the occurrence of relatively high concentrations of CH_4, which, on the contrary, did not show any anomalous concentrations in the other measurements sites near the hydrothermal emissions (i.e. FU, AC and GW). On the whole, the H_2S–CO_2 pair has proved to be a successful tracer to investigate the spatial distribution of hydrothermal gases in air in the proximity of hydrothermal emission spots, the latter being dependent on (i) dilution by mixing with air and (ii) consumption processes, mostly affecting H_2S through oxidation to SO_2. In fact, SO_2 concentrations measured at FU, AC and GW and HT were found to be strongly related to those of H_2S. At DS, i.e. the measurement site located at about 800 m from the Pisciarelli fumarolic emissions, the main hydrothermal tracers (CO_2 and H_2S) were completely masked by anthropogenic sources. Accordingly, anomalously high SO_2 concentrations were interpreted as related to anthropogenic activities, being not accompanied by H_2S.

The results of this study evidence that the hydrothermal emissions discharged by the under-construction geothermal well at the GW site had a significant impact on local air quality, leading to a dramatic increase of CO_2 and H_2S concentrations (up to 1,061 mg/m^3 and 1,570 μg/m^3, respectively) in a densely inhabited zone of Pozzuoli town. Such evidence claimed the attention of local competent authorities which suspended the well construction. It is worth noting that, although CO_2

concentrations in air remained well below the alert threshold of 0.5% (OSHA, 2019), the H_2S concentrations were up to 3 orders of magnitude higher than those of the urban background (1–3 μg/m^3; Kourtidis et al., 2008), occasionally exceeding the threshold values suggested by the WHO (2000) for prolonged exposures, i.e. 150 μg/m^3 for exposures up to 24 h, 100 μg/m^3 for exposures >14 days, and 20 μg/m^3 for exposures >90 days (average values during the period). This situation may pose a potential hazard for the local population, especially when weather conditions. i.e. low wind and cloudy sky, favor the accumulation of H_2S in depressed areas and/or enclosed spaces.

Despite the evident results reported, the very short measurement periods and the unsynchronous sampling strategy are the limits of this study. Nevertheless, the expeditious approach adopted has demonstrated that this geochemical survey is potentially useful to both discriminate the origin of pollutant gases and enquire into their possible impact on air quality. However, in order to extend these results over time and space, and to further understand the physicochemical processes involving the distribution of these gases in air, it may be necessary to simultaneously measure over longer periods in the selected sites.

Author statement

Rebecca Biagi: Conceptualization, Data curation, Writing – original draft, Formal analysis, Investigation, Visualization. **Franco Tassi**: Conceptualization, Methodology, Validation, Writing- Reviewing and Editing, Supervision. **Stefano Caliro**: Conceptualization, Writing – review & editing, Supervision. **Francesco Capecchiacci**: Writing – review & editing, Investigation, Methodology. **Stefania Venturi**: Conceptualization, Writing – review & editing, Data curation.

Declaration of competing interest

The authors declare that they have no known competing financial interests or personal relationships that could have appeared to influence the work reported in this paper.

Acknowledgments

The authors wish to thank Tennis Hotel, Autouno Volkswagen garage service, Max Sporting Club, Genny, and particularly Osservatorio Vesuviano (INGV, Sezione di Napoli), for having provided access to the measuring sites, logistical support and energy supply. A. Santi is kindly acknowledged for his help during the measuring campaigns.

Appendix A. Supplementary data

Supplementary data to this article can be found online at https://doi.org/10.1016/j.chemosphere.2022.134166.

References

AdminStat, 2020. https://ugeo.urbistat.com/AdminStat/it/it/demografia/dati-sintesi/pozzuoli/63060/4.

Aiuppa, A., 2015. Volcanic-gas monitoring. In: Schmidt, A., Fristad, K., Elkins-Tanton, L. (Eds.), Volcanism and Global Environmental Change. Cambridge University Press, pp. 81–96. https://doi.org/10.1017/CBO9781107415683.009.

Aiuppa, A., Giudice, G., Gurrieri, S., Liuzzo, M., Burton, M., Caltabiano, T., McGonigle, A. J.S., Salerno, G., Shinohara, H., Valenza, M., 2008. Total volatile flux from Mount Etna. Geophys. Res. Lett. 35, L24302. https://doi.org/10.1029/2008GL035871.

Aiuppa, A., Tamburello, G., Di Napoli, R., Cardellini, C., Chiodini, G., Giudice, G., Grassa, F., Pedone, M., 2013. First observations of the fumarolic gas output from a restless caldera: implications for the current period of unrest (2005–2013) at Campi Flegrei. Geochem. Geophys. 14 (10), 4153–4169. https://doi.org/10.1002/ggge.20261.

Allard, P., Carbonnelle, J., Dajlevic, D., Le Bronec, J., Morel, P., Robe, M.C., Maurenas, J. M., Faivre-Pierret, R., Martin, D., Sabroux, J.C., Zettwoog, P., 1991. Eruptive and diffuse emissions of CO_2 from Mount Etna. Nature 351, 387–391. https://doi.org/10.1038/351387a0.

Allard, P., Carbonnelle, J., Métrich, N., Loyer, H., Zettwoog, P., 1994. Sulphur output and magma degassing budget of Stromboli volcano. Nature 368, 326–330. https://doi.org/10.1038/368326a0.

Andres, R.J., Kasgnoc, A.D., 1998. A time-averaged inventory of subaerial volcanic sulfur emissions. J. Geophys. Res. 103 (D19) https://doi.org/10.1029/98JD02091, 25,251-25,261.

Badalamenti, B., Liotta, M., Valenza, M., 2001. An automatic system for continuous monitoring of CO_2, H_2S, SO_2 and meteorological parameters in the atmosphere of volcanic areas. Geochem. Trans. 5 https://doi.org/10.1039/B104622P.

Barberi, F., Corrado, G., Innocenti, F., Luongo, G., 1984. Phlegraean fields 1982-1984: brief chronicle of a volcano emergency in a densely populated area. Bull. Volcanol. 47 (2), 175–185. https://doi.org/10.1007/BF01961547.

Bartlett, K.B., Harriss, R.C., 1993. Review and assessment of methane emissions from wetlands. Chemosphere 26 (l-4), 261–320. https://doi.org/10.1016/0045-6535(93)90427-7.

Baubron, J.C., Allard, P., Toutain, J.P., 1990. Diffuse volcanic emissions of carbon dioxide from Vulcano Island, Italy. Nature 344, 51–53. https://doi.org/10.1038/344051a0.

Bonafede, M., Mazzanti, M., 1998. Modelling gravity variations consistent with ground deformation in the Campi Flegrei caldera (Italy). J. Volcanol. Geoth. Res. 81, 137–157. https://doi.org/10.1016/S0377-0273(97)00071-1.

Burton, M.R., Oppenheimer, C., Horrocks, L.A., Francis, P.W., 2000. Remote sensing of CO_2 and H_2O emission rates from Masaya volcano. Nicaragua. Geology 28, 915–918. https://doi.org/10.1130/0091-7613(2000)28<915:RSOCAH>2.0.CO;2.

Burton, M.R., Sawyer, G.M., Granieri, D., 2013. Deep carbon emissions from volcanoes. Rev. Mineral. Geochem. 75, 323–354. https://doi.org/10.2138/rmg.2013.75.11.

Cabassi, J., Tassi, F., Venturi, S., Calabrese, S., Capecchiacci, F., D'Alessandro, W., Vaselli, O., 2017. A new approach for the measurement of gaseous elemental mercury (GEM) and H_2S in air from anthropogenic and natural sources: examples from Mt. Amiata (Siena, Central Italy) and Solfatara Crater (Campi Flegrei, Southern Italy). J. Geochem. Explor. 175, 48–58. https://doi.org/10.1016/j.gexplo.2016.12.017.

Calabrese, S., Randazzo, L., Daskalopoulou, K., Milazzo, S., Scaglione, S., Vizzini, S., Tramati, C.D., D'Alessandro, W., Brusca, L., Bellomo, S., Giuffrida, G.B., Pecoraino, G., Montana, G., Salerno, G., Giammanco, S., Catalbiano, T., Parello, F., 2016. Mount Etna volcano (Italy) as a mayor "dust" point source in the Mediterranean area. Arabian J. Geosci. 9, 219. https://doi.org/10.1007/s12517-015-2165-0.

Caliro, S., Chiodini, G., Moretti, R., Avino, R., Granieri, D., Russo, M., Fiebig, J., 2007. The origin of the fumaroles of La Solfatara (Campi Flegrei, south Italy). Geochem. Cosmochim. Acta 71, 3040–3055. https://doi.org/10.1016/j.gca.2007.04.007.

Carapezza, M.L., Gurrieri, S., Nuccio, P.M., Valenza, M., 1984. CO_2 and H_2S concentrations in the atmosphere at the Solfatara of Pozzuoli. BulI. Volcanol. 47 (2), 287–293. https://doi.org/10.1007/BF01961559.

Carapezza, M.L., Badalamenti, B., Cavarra, L., Scalzo, A., 2003. Gas hazard assessment in a densely inhabited area of Colli Albani Volcano (Cava dei Selci, Roma). J. Volcanol. Geoth. Res. 123, 81–94. https://doi.org/10.1016/S0377-0273(03)00029-5.

Cardellini, C., Chiodini, G., Frondini, F., Avino, R., Bagnato, E., Caliro, S., Lelli, M., Rosiello, A., 2017. Monitoring diffuse volcanic degassing during volcanic unrests: the case of Campi Flegrei (Italy). Sci. Rep. 7 (1) https://doi.org/10.1038/s41598-017-06941-2.

Carlson, C.A., Bates, N.R., Hansell, D.A., Steinberg, D.K., 2001. Carbon cycle. In: Encyclopedia of Ocean Sciences, second ed. Elsevier Inc, pp. 477–486. https://doi.org/10.1016/B978-012374473-9.00272-1.

Carslaw, D.C., 2014. The Openair Manual — Open-Source Tools for Analyzing Air Pollution Data. King's College, London. Manual for Version 1.0.

Carslaw, D.C., Ropkins, K., 2012. Openair — an R package for air quality data analysis. Environ. Model. Software 27–28, 52–61. https://doi.org/10.1016/j.envsoft.2011.09.008.

Chamberlain, S.D., Ingraffea, A.R., Sparks, J.P., 2016. Sourcing methane and carbon dioxide emissions from a small city: influence of natural gas leakage and combustion. Environ. Pollut. 218, 102–111. https://doi.org/10.1016/j.envpol.2016.08.036.

Chiodini, G., Caliro, S., De Martino, P., Avino, R., Gherardi, F., 2012. Early signals of new volcanic unrest at Campi Flegrei caldera? Insights from geochemical data and physical simulations. Geology 40, 943–946. https://doi.org/10.1130/G33251.1.

Chiodini, G., Vandemeulebrouck, J., Caliro, S., D'Auria, L., De Martino, P., Mangiacapra, A., Petrillo, Z., 2015. Evidence of thermal-driven processes triggering the 2005–2014 unrest at Campi Flegrei caldera. EPSL 414, 58–67. https://doi.org/10.1016/j.epsl.2015.01.012.

Chiodini, G., Selva, J., Del Pezzo, E., Marsan, D., De Siena, L., D'Auria, L., Bianco, F., Caliro, S., De Martino, P., Ricciolino, P., Petrillo, Z., 2017. Clues on the origin of post-2000 earthquakes at Campi Flegrei caldera (Italy). Sci. Rep. 7 (1), 1–10. https://doi.org/10.1038/s41598-017-04845-9.

De Vivo, B., Rolandi, G., Gans, P.B., Calvert, A., Bohrson, W.A., Spera, F.J., Belkin, H.E., 2001. New constraints on the pyroclastic eruptive history of the Campanian volcanic Plain (Italy). Mineral. Petrol. 73, 47–65. https://doi.org/10.1007/s007100170010.

Deino, A.L., Orsi, G., de Vita, S., Piochi, M., 2004. The age of the Neapolitan Yellow Tuff caldera-forming eruption (Campi Flegrei caldera - Italy) assessed by $^{40}Ar/^{39}Ar$ dating method. J. Volcanol. Geoth. Res. 133, 157–170. https://doi.org/10.1016/S0377-0273(03)00396-2.

Delmelle, P., Stix, J., Baxter, P.J., Garcia-Alvarez, J., Barquero, J., 2002. Atmospheric dispersion, environmental effects and potential health hazard associated with the low-altitude gas plume of Masaya volcano, Nicaragua. Bull. Volcanol. 64, 423–434. https://doi.org/10.1007/s00445-002-0221-6.

Di Vito, M., Lirer, L., Mastrolorenzo, G., Rolandi, G., 1987. The 1538 monte Nuovo eruption (Campi Flegrei, Italy). Bull. Volcanol. 49, 608–615. https://doi.org/10.1007/BF01079966.

Dlugokencky, E., 2021. NOAA/ESRL. www.esrl.noaa.gov/gmd/ccgg/trends_ch4/.

Fisher Scientific Inc, Thermo, 2012. Thermo Scientific Model 450*i* Hydrogen Sulfide & Sulfur Dioxide Analyzer Manual. https://www.thermofisher.com/content/dam/tfs/ATG/EPD/EPD_Documents/Product_Manuals_&_Specifications/Air_Quality_Instruments_and_Systems/Ambient_Gas/D19731~.pdf.

Florio, G., Fedi, M., Cella, F., Rapolla, A., 1999. The Campanian Plain and Phlegrean Fields: structural setting from potential field data. J. Volcanol. Geoth. Res. 91, 361–379. https://doi.org/10.1016/S0377-0273(99)00044-X.

Gerlach, T., 2011. Volcanic versus anthropogenic carbon dioxide. EOS 92 (24), 201–208. https://doi.org/10.1029/2011EO240001.

Giggenbach, W.F., 1996. Chemical composition of volcanic gases. In: Monitoring and Mitigation of Volcano Hazards. Springer Verlag, Berlin, pp. 222–256. https://doi.org/10.1007/978-3-642-80087-0_7.

Girona, T., Costa, F., Newhall, C., Taisne, B., 2014. On depressurization of volcanic magma reservoirs by passive degassing. J. Geophys. Res. Solid Earth 119, 8667–8687. https://doi.org/10.1002/2014JB011368.

Granieri, D., Avino, R., Chiodini, G., 2009. Carbon dioxide diffuse emission from the soil: ten years of observations at Vesuvio and Campi Flegrei (Pozzuoli), and linkages with volcanic activity. Bull. Volcanol. 72, 103–118. https://doi.org/10.1007/s00445-009-0304-8.

Hansen, J., Lacis, A., Ruedy, R., Sato, M., 1992. Potential climate impact of Mount Pinatubo eruption. Geophys. Res. Lett. 19 (2), 215–218. https://doi.org/10.1029/91GL02788.

Holmes, C.D., 2018. Methane feedback on atmospheric chemistry: methods, models, and mechanisms. J. Adv. Model. Earth Syst. 10, 1087–1099. https://doi.org/10.1002/2017MS001196.

Horwell, C.J., Baxter, P.J., 2006. The respiratory health hazards of volcanic ash: a review for volcanic risk mitigation. Bull. Volcanol. 69 (1), 1–24. https://doi.org/10.1007/s00445-006-0052-y.

Ingv-Ov, 2020. Perforazioni Per Pozzo Geotermico Area Campi Flegrei – Progetto Geogrid. Istituto Nazionale di Geofisica e Vulcanologia AOO INGV Protocollo Generale – U N, 0006939 del 17/06/2020.

Isaia, R., Marianelli, P., Sbrana, A., 2009. Caldera unrest prior to intense volcanism in Campi Flegrei (Italy) at 4.0 ka B.P.: implications for caldera dynamics and future eruptive scenarios. Geophys. Res. Lett. 36, L21303. https://doi.org/10.1029/2009GL040513.

Keeling, C.D., 1958. The concentration and isotopic abundances of atmospheric carbon dioxide in rural areas. Geochem. Cosmochim. Acta 13, 322–334. https://doi.org/10.1016/0016-7037(58)90033-4.

Keeling, C.D., 1961. The concentration and isotopic abundance of carbon dioxide in rural and marine air. Geochem. Cosmochim. Acta 24, 277–298. https://doi.org/10.1016/0016-7037(61)90023-0.

Kelly, P.M., Sear, C.B., 1984. Climatic impact of explosive volcanic eruptions. Nature 311, 740–743. https://doi.org/10.1038/311740a0.

Kestrel®, 2020. Kestrel® 4500 datasheet. https://cdn.shopify.com/s/files/1/0084/9012/files/Kestrel_CoC.pdf?1810.

Kourtidis, K., Kelesis, A., Petrakakis, M., 2008. Hydrogen sulfide (H_2S) in urban ambient air. Atmos. Environ. 42, 7476–7482. https://doi.org/10.1016/j.atmosenv.2008.05.066.

Levin, I., Bergamaschi, P., Dörr, H., Trapp, D., 1993. Stable isotopic signature of methane from major sources in Germany. Chemosphere 26 (1–4), 161–177. https://doi.org/10.1016/0045-6535(93)90419-6.

Llavador Colomer, F., Espinós Morató, H., Mantilla Iglesias, E., 2012. Estimation of hydrogen sulfide emission rates at several wastewater treatment plants through experimental concentration measurements and dispersion modeling. J. Air Waste Manag. Assoc. 62 (7), 758–766. https://doi.org/10.1080/10962247.2012.674008.

Lowry, D., Holmes, C.W., Rata, N.D., O'Brien, P., Nisbet, E.G., 2001. London methane emissions: use of diurnal changes in concentration and $\delta^{13}C$ to identify urban sources and verify inventories. J. Geophys. Res. 106 (D7), 7427–7448. https://doi.org/10.1029/2000JD900601.

Malowany, K., Stix, J., Van Pelt, A., Lucic, G., 2015. H_2S interference on CO_2 isotopic measurements using a Picarro G1101-*i* cavity ring-down spectrometer. Atmos. Meas. Tech. 8, 4075–4082. https://doi.org/10.5194/amt-8-4075-2015.

Martin, R.S., Sawyer, G.M., Spampinato, L., Salerno, G.G., Ramirez, C., Ilyinskaya, E., Witt, M.L.I., Mather, T.A., Watson, I.M., Phillips, J.C., Oppenheimer, C., 2010. A total volatile inventory for Masaya Volcano, Nicaragua. J. Geophys. Res. 115, B09215. https://doi.org/10.1029/2010JB007480.

McCormick, M.P., Thomason, L.W., Trepte, C.R., 1995. Atmospheric effects of the Mt Pinatubo eruption. Nature 373, 399–404. https://doi.org/10.1038/373399a0.

McGee, K.A., Doukas, M.P., Kessler, R., Gerlach, T.M., 1997. Impacts of Volcanic Gases on Climate, the Environment, and People. U.S. Geological Survey Open-File Report 97-262. https://pubs.usgs.gov/openfile/of97-262/of97-262.html.

Monks, P.S., Granier, C., Fuzzi, S., Stohl, A., Williams, M.L., Akimoto, H., Amanni, M., Baklanov, A., Baltensperger, U., Bey, I., Blake, N., Blake, R.S., Carslawn, K., Cooper, O.R., Dentener, F., Fowler, D., Fragkou, E., Frost, G.J., Generoso, S., Ginoux, P., Grewet, V., Guenther, A., Hansson, H.C., Hennew, S., Hjorth, J., Hofzumahaus, A., Huntrieser, H., Isaksen, I.S.A., Jenkin, M.E., Kaiser, J., Kanakidou, M., Klimont, Z., Kulmala, M., Laj, P., Lawrence, M.G., Lee, J.D., Liousse, C., Maione, M., McFiggans, G., Metzger, A., Mieville, A., Moussiopoulos, N., Orlando, J.J., O'Dowd, C.S., Palmer, P.I., Parrish, D.D., Petzold, A., Platt, U., Pöschl, U., Prévôt, A.S.H., Reeves, C.E., Reimannw, S., Rudich, Y., Sellegri, K., Steinbrecher, S., Simpson, D., ten Brink, H., Theloke, J., van der Werf, G.R., Vautard, R., Vestreng, V., Vlachokostas, Ch, von Glasowbb, R., 2009. Atmospheric composition change – global and regional air quality. Atmos. Environ. 43, 5268–5350. https://doi.org/10.1016/j.atmosenv.2009.08.021.

Mörner, N.A., Etiope, G., 2002. Carbon degassing from the lithosphere. Global Planet. Change 33, 185–203. https://doi.org/10.1016/S0921-8181(02)00070-X.

Nys Department of Health, 2005. Hydrogen Sulfide Chemical Information Sheet. https://www.health.ny.gov/environmental/chemicals/hydrogen_sulfide/.

Oppenheimer, C., 2003. Climatic, environmental and human consequences of the largest known historic eruption: tambora volcano (Indonesia) 1815. Prog. Phys. Geogr. 27 (2), 230–259. https://doi.org/10.1191/0309133303pp379ra.

Orsi, G., De Vita, S., Di Vito, M., 1996. The restless, resurgent Campi Flegrei nested caldera (Italy): constraints on its evolution and configuration. J. Volcanol. Geoth. Res. 74, 179–214. https://doi.org/10.1016/S0377-0273(96)00063-7.

Orsi, G., Di Vito, M., Isaia, R., 2004. Volcanic hazard assessment at the restless Campi Flegrei caldera. Bull. Volcanol. 66, 514–530. https://doi.org/10.1007/s00445-003-0336-4.

OSHA, 2019. Carbon Dioxide Health Hazard Information Sheet. FSIS Environmental, Safety and Health Group. https://www.osha.gov/chemicaldata/chemResult.html?recNo=183.

Pataki, D.E., Ehleringer, J.R., Flanagan, L.B., Yakir, D., Bowling, D.R., Still, C.J., Buchmann, N., Kaplan, J.O., Berry, J.A., 2003. The application and interpretation of Keeling plots in terrestrial carbon cycle research. Global Biogeochem. Cycles 17 (1), 1022. https://doi.org/10.1029/2001GB001850.

Quay, P., King, S.L., Lansdown, J.M., Wilbur, D.O., 1988. Isotopic composition of methane released from wetlands: implications for the increase in atmospheric methane. Global Biogeochem. Cycles 2 (4), 385–397. https://doi.org/10.1029/GB002i004p00385.

Quay, P., Stutsmann, J., Wilbur, D., Snover, A., Dlugokencky, E., Brown, T., 1999. The isotopic composition of atmospheric methane. Global Biogeochem. Cycles 13 (2), 445–461.

Queißer, M., Granieri, D., Burton, M., Arzilli, F., Avino, R., Carandente, A., 2017. Increasing CO_2 flux at Pisciarelli, Campi Flegrei, Italy. Solid Earth 8 (5), 1017–1024 https://doi.org/10.519/se-8-1017-2017.

R Core Team, 2017. R: A Language and Environment for Statistical Computing. https://www.R-project.org/.

Raible, C.C., Brönnimann, S., Auchmann, R., Brohan, P., Frölicher, T.L., Graf, H.F., Jones, P., Luterbacher, J., Muthers, S., Neukom, R., Robock, A., Self, S., Sudrajat, A., Timmreck, C., Wegmann, M., 2016. Tambora 1815 as a test case for high impact volcanic eruptions: earth system effects. WIREs Clim. Change 7, 569–589. https://doi.org/10.1002/wcc.407.

Rampino, M.R., Self, S., 1982. Historic eruptions of tambora (1815), krakatau (1883), and agung (1963), their stratospheric aerosols, and climatic impact. Quat. Res. 18, 127–143. https://doi.org/10.1016/0033-5894(82)90065-5.

Reikard, G., 2019. Volcanic emissions and air pollution: forecasts from time series models. Atmos. Environ. 1, 100001. https://doi.org/10.1016/j.aeaoa.2018.100001.

Riebeek, H., Simmon, R., 2011. The Carbon Cycle. https://earthobservatory.nasa.gov/features/CarbonCycle.

Robock, A., 1981. The mount st. Helens volcanic eruption of 18 may 1980: minimal climatic effect. Science 212, 1383–1384. https://doi.org/10.1126/science.212.4501.1383.

Robock, A., 2000. Volcanic eruptions and climate. Rev. Geophys. 38, 191–219. https://doi.org/10.1029/1998RG000054.

Robock, A., 2004. Climatic impact of volcanic emissions. In: Sparks, R.S.J., Hawkesworth, C.J. (Eds.), State of the Planet: Frontiers and Challenges in Geophysics, vol. 150. AGU Geophysical Monograph, pp. 125–134. https://doi.org/10.1029/150GM11.

Rubright, S.L.M., Pearce, L.L., Peterson, J., 2017. Environmental toxicology of hydrogen sulfide. Nitric Oxide 71, 1–13. https://doi.org/10.1016/j.niox.2017.09.011.

Saunois, M., Stavert, A.R., Poulter, B., Bousquet, P., Canadell, J.G., Jackson, R.B., Raymond, P.A., Dlugokencky, E.J., Houweling, S., Patra, P.K., Ciais, P., Arora, V.K., Bastviken, D., Bergamaschi, P., Blake, D.R., Brailsford, G., Bruhwiler, L., Carlson, K. M., Carrol, M., Castaldi, S., Chandra, N., Crevoisier, C., Crill, P.M., Covey, K., Curry, C.L., Etiope, G., Frankenberg, C., Gedney, N., Hegglin, M.I., Höglund-Isaksson, L., Hugelius, G., Ishizawa, M., Ito, A., Janssens-Maenhout, G., Jensen, K.M., Joos, F., Kleinen, T., Krummel, P.B., Langenfelds, R.L., Laruelle, G.G., Liu, L., Machida, T., Maksyutov, S., McDonald, K.C., McNorton, J., Miller, P.A., Melton, J.R., Morino, I., Müller, J., Murguia-Flores, F., Naik, V., Niwa, Y., Noce, S., O'Doherty, S., Parker, R.J., Peng, C., Peng, S., Peters, G.P., Prigent, C., Prinn, R., Ramonet, M., Regnier, P., Riley, W.J., Rosentreter, J.A., Segers, A., Simpson, I.J., Shi, H., Smith, S. J., Steele, L.P., Thornton, B.F., Tian, H., Tohjima, Y., Tubiello, F.N., Tsuruta, A., Viovy, N., Voulgarakis, A., Weber, T.S., van Weele, M., van der Werf, G.R., Weiss, R. F., Worthy, D., Wunch, D., Yin, Y., Yoshida, Y., Zhang, W., Zhang, Z., Zhao, Y., Zheng, B., Zhu, Q., Zhu, Q., Zhuang, Q., 2019. The global methane budget 2000-2017. Earth Syst. Sci. Data. https://doi.org/10.5194/essd-2019-128.

Schwietzke, S., Sherwood, O.A., Bruhwiler, L.M.P., Miller, J.B., Etiope, G., Dlugokencky, E.J., Englund Michel, S., Arling, V.A., Vaughn, B.H., White, J.W.C., Tans, P.P., 2016. Upward revision of global fossil fuel methane emissions based on isotope database. Nature 538, 88–91. https://doi.org/10.1038/nature19797.

Self, S., 2005. Effects of volcanic eruptions on the atmosphere and climate. In: Martí, J., Ernst, G.G.J. (Eds.), Volcanoes and the Environment. Cambridge University Press, pp. 152–174.

Self, S., 2006. The effects and consequences of very large explosive volcanic eruptions. Philos. Trans. R. Soc. A 364, 2073–2097. https://doi.org/10.1098/rsta.2006.1814.

Self, S., Zhao, J.X., Holasek, R.E., Torres, R.C., King, A.J., 1993. The Atmospheric Impact of the 1991 Mount Pinatubo Eruption. NASA/CR93-207274.

Self, S., Gertisser, R., Thordarson, T., Rampino, M.R., Wolff, J.A., 2004. Magma volume, volatile emissions, and stratospheric aerosols from the 1815 eruption of Tambora. Geophys. Res. Lett. 31, L20608. https://doi.org/10.1029/2004GL020925.

Sherwood, O.A., Schwietzke, S., Arling, V.A., Etiope, G., 2017. Global inventory of gas geochemistry data from fossil fuel, microbial and burning sources, version 2017. Earth Syst. Sci. Data 9, 639–656. https://doi.org/10.5194/essd-9-639-2017.

Tamburello, G., Caliro, S., Chiodini, G., De Martino, P., Avino, R., Minopoli, C., Carandente, A., Rouwet, D., Aiuppa, A., Costa, A., Bitetto, M., Giudice, G., Francofonte, V., Ricci, T., Sciarra, A., Bagnato, E., Capecchiacci, F., 2019. Escalating CO_2 degassing at the Pisciarelli fumarolic system, and implications for the ongoing Campi Flegrei unrest. J. Volcanol. Geoth. Res. 384, 151–157. https://doi.org/10.1016/j.jvolgeores.2019.07.005.

Tassi, F., Vaselli, O., Cuccoli, F., Buccianti, A., Nisi, B., Lognoli, E., Montegrossi, G., 2009. A geochemical multi-methodological approach in hazard assessment of CO_2-rich gas emissions at Mt. Amiata volcano (Tuscany, central Italy). Water, Air. Soil Pollution Focus 9, 117–127. https://doi.org/10.1007/s11267-008-9198-2.

Tassi, F., Nisi, B., Cardellini, C., Capecchiacci, F., Donnini, M., Vaselli, O., Avino, R., Chiodini, G., 2013. Diffuse soil emission of hydrothermal gases (CO_2, CH_4, and C_6H_6) at Solfatara crater (Campi Flegrei, southern Italy). Appl. Geochem. 35, 142–153. https://doi.org/10.1016/j.apgeochem.2013.03.020.

Tassi, F., Venturi, S., Cabassi, J., Capecchiacci, F., Nisi, B., Vaselli, O., 2015. Volatile organic compounds (VOCs) in soil gases from Solfatara crater (Campi Flegrei, southern Italy): geogenic source(s) vs. biogeochemical processes. Appl. Geochem. 56, 37–49. https://doi.org/10.1016/j.apgeochem.2015.02.005.

Textor, C., Graf, H.F., Herzog, M., Oberhuber, J.M., 2003. Injection of gases into the stratosphere by explosive volcanic eruptions. J. Geophys. Res. 108, 4606. https://doi.org/10.1029/2002JD002987.

Thorsteinsson, T., Hackenbruch, J., Sveinbjörnsson, E., Jóhannsson, T., 2013. Statistical assessment and modeling of the effects of weather conditions on H_2S plume dispersal from Icelandic geothermal power plants. Geothermics 45, 31–40.

Townsend-Small, A., Tyler, S.C., Pataki, D.E., Xu, X., Christensen, L.E., 2012. Isotopic measurements of atmospheric methane in Los Angeles, California, USA: influence of "fugitive" fossil fuel emissions. J. Geophys. Res. 117, D07308. https://doi.org/10.1029/2011JD016826.

Vaselli, O., Nisi, B., Tassi, F., Rappuoli, D., Pancioli, V., Ucciero, S., Giannini, L., 2011. CO_2 hazard vs touristic attraction at the Mt. Amiata Volcano (Italy). Acta Vulcanol. 23 (1–2), 73–80.

Venturi, S., Cabassi, J., Tassi, F., Capecchiacci, F., Vaselli, O., Bellomo, S., Calabrese, S., D'Alessandro, W., 2016. Hydrogen sulfide measurements in air by passive/diffusive samplers and high-frequency analyzer: a critical comparison. Appl. Geochem. 72, 51–58. https://doi.org/10.1016/j.apgeochem.2016.07.001.

Venturi, S., Tassi, F., Cabassi, J., Vaselli, O., Minardi, I., Neri, S., Caponi, C., Capasso, G., Di Martino, R.M.R., Ricci, A., Capecchiacci, F., Lelli, M., Sciarra, A., Cinti, D., Virgili, G., 2019. A multi-instrumental geochemical approach to assess the environmental impact of CO_2-rich gas emissions in a densely populated area: the case of Cava dei Selci (Latium, Italy). Appl. Geochem. 101, 109–126. https://doi.org/10.1016/j.apgeochem.2019.01.003.

Venturi, S., Tassi, F., Cabassi, J., Gioli, B., Baronti, S., Vaselli, O., Caponi, C., Vagnoli, C., Picchi, G., Zaldei, A., Magi, F., Miglietta, F., Capecchiacci, F., 2020. Seasonal and diurnal variations of greenhouse gases in Florence (Italy): inferring sources and sinks from carbon isotopic ratios. STOTEN 698, 134245. https://doi.org/10.1016/j.scitotenv.2019.134245.

Venturi, S., Cabassi, J., Tassi, F., Maioli, G., Randazzo, A., Capecchiacci, F., Vaselli, O., 2021. Near-surface atmospheric concentrations of greenhouse gases (CO_2 and CH_4) in Florence urban area: inferring emitting sources through carbon isotopic analysis. Urban Clim. 39, 100968. https://doi.org/10.1016/j.uclim.2021.100968.

Vilardo, G., Alessio, G., Luongo, G., 1991. Analysis of the magnitude-frequency distribution for the 1983– 1984 earthquake activity of Campi Flegrei. Italy. J. Volcanol. Geotherm. Res. 48 (1–2), 115–125. https://doi.org/10.1016/0377-0273(91)90037-Z.

Viveiros, F., Cardellini, C., Ferreira, T., Caliro, S., Chiodini, G., Silva, C., 2010. Soil CO_2 emissions at Furnas Volcano, São Miguel Island, Azores archipelago: volcano monitoring perspectives, geomorphologic studies, and land use planning application. J. Geophys. Res. 115, B12208. https://doi.org/10.1029/2010JB007555.

von Glasow, R., Bobrowski, N., Kern, C., 2009. The effects of volcanic eruptions on atmospheric chemistry. Chem. Geol. 263, 131–142. https://doi.org/10.1016/j.chemgeo.2008.08.020.

Who, 1981. Hydrogen Sulfide. In: Environmental Health Criteria, 19. World Health Organization, Geneva, Switzerland. http://www.inchem.org/documents/ehc/ehc/ehc019.htm.

Who, 2000. Hydrogen Sulfide, second ed. In: Air Quality Guidelines for Europe. © WHO Regional Office for Europe, Copenhagen, Denmark https://www.euro.who.int/_data/assets/pdf_file/0005/74732/E71922.pdf.

Who, 2003. Hydrogen Sulfide: Human Health Aspects. In: Concise International Chemical Assessment Document 53. World Health Organization, Geneva, Switzerland. https://www.who.int/ipcs/publications/cicad/en/cicad53.pdf.

Who, 200b. Sulfur Dioxide. Air Quality Guidelines for Europe - second ed.. © WHO Regional Office for Europe, Copenhagen, Denmark. https://www.euro.who.int/_data/assets/pdf_file/0020/123086/AQG2ndEd_7_4Sulfurdioxide.pdf.

Who, 2018. Ambient (Outdoor) Air Pollution. https://www.who.int/news-room/fact-sheets/detail/ambient-(outdoor)-airquality-and-health.

Zazzeri, G., Lowry, D., Fisher, R.E., France, J.L., Lanoisellé, M., Grimmond, C.S.B., Nisbet, E.G., 2017. Evaluating methane inventories by isotopic analysis in the London region. Sci. Rep. 7, 4854. https://doi.org/10.1038/s41598-017-04802-6.

Zobitz, J.M., Keener, J.P., Schnyder, H., Bowling, D.R., 2006. Sensitivity analysis and quantification of uncertainty for isotopic mixing relationships in carbon cycle research. Agric. For. Meteorol. 136, 56–75. https://doi.org/10.1016/j.agrformet.2006.01.003.